

~~Earth system models overestimate the sensitivity of apparent oxygen utilisation to age change in the deep ocean~~ Divergent Sensitivities of Apparent Oxygen Utilization to Circulation Changes in the Deep Ocean Across Earth System Models

*Damien Couespel^a, Xabier Davila^a, Nadine Goris^a, Emil Jeansson^a, Siv K. Lauvset^a, Jerry Tjiputra^a

^aNORCE Research AS, Bjerknes Centre for Climate Research, Bergen, Norway

Corresponding author: daco@norceresearch.no

Abstract

The biological carbon pump (BCP), involving photosynthesis at the surface and remineralisation at depth, maintains a significant vertical gradient in dissolved inorganic carbon (DIC), thereby promoting the ocean's ability to absorb atmospheric CO₂. Remineralised DIC is a good indicator of the strength of the BCP. It can be estimated from apparent oxygen utilisation (AOU) ~~that~~, which measures the deficit of oxygen ~~compared~~ relative to saturation. AOUs are projected to increase under climate change due to changes in remineralisation rates and circulation. However, the amplitude of the change ~~is still~~ remains uncertain. Here, we identify linear relationships between ~~AOU trends and age trends~~ trends in AOUs and ideal-age in the deep ocean ~~in~~, based on simulations of the contemporary (~~1972-2013~~ 1982-2013) and future (2015-2099) periods from five Earth system models (ESMs). ~~Linear relationships identified within observational data for the contemporary period indicate that ESMs overestimate the sensitivity of AOUs to age changes in the deep ocean~~ Our analysis underscores the substantial role of circulation slowdown in increasing remineralised DIC. The study highlights the stability over time of the AOUs sensitivity ~~Furthermore, the study highlights considerable inter-model variability in their sensitivity of AOUs to age changes, suggesting an overestimation of the BCP strengthening inferred from AOUs with this sensitivity remaining relatively stable over time. Furthermore, our analysis underestimates the substantial role of circulation slowdown in increasing remineralised DIC~~ With more observational data, refined estimates of age changes from ocean tracers and a larger model ensemble, constraining this variability will become feasible. These insights emphasise both the challenges and opportunities ~~to constrain~~ for constraining future BCP projections ~~due to~~ circulation uncertainties ~~arising from uncertainties in circulation.~~

25 Introduction

26 1 Introduction

27 The capacity of the ocean to take up and store carbon is driven by the marine carbonate chemistry, the solubility pump and
28 the biological carbon pump (BCP hereafter, accounting for the carbonate and soft-tissue pumps, Volk and Hoffert (1985)
29 and see DeVries (2022) for a review of the ocean carbon cycle). A part of the BCP is the photosynthetic transformation of
30 inorganic carbon to organic carbon at the surface. The organic material is then transported to depth where it is transformed
31 back into its inorganic form through ~~rem mineralization~~rem mineralisation. In the deep ocean, remineralised carbon and nutrients are
32 accumulated. This accumulation is an important component of the BCP and is connected to the strength of the ocean ~~circulation~~.
33 ~~Then, overturning circulation, which transports the~~ inorganic carbon and nutrients ~~are transported~~ back to the surface, closing
34 the loop. The BCP is ~~thought to be therefore the primary mechanism~~ responsible for keeping the concentration of dissolved
35 inorganic carbon (DIC) low at the surface ~~low and high in the interior~~, resulting in a large vertical gradient of DIC (Volk and
36 Hoffert, 1985; Boyd et al., 2019; DeVries, 2022) ~~with more DIC in the deep ocean~~. This enhances the capacity of the ocean to
37 take up atmospheric CO₂ (Kwon et al., 2009). Without the BCP, atmospheric CO₂ would be more than 200 ppm higher ~~than~~
38 otherwise (Sarmiento and Toggweiler, 1984; Maier-Reimer et al., 1996; Goodwin et al., 2008; Tjiputra et al., 2025).

39 Due to competition between the decrease in organic matter export and slower circulation, it is unclear how the role of BCP
40 will change in the future (Frenger et al., 2024). There is a general consensus between state-of-the-art Earth system mod-
41 els (ESMs) that the BCP and the processes involved are impacted by global warming (Wilson et al., 2022), but the ampli-
42 tude of the change and its response to higher atmospheric CO₂ are both still uncertain. Indicators of the functionality
43 of the BCP are primary production (related to the photosynthetic transformation of carbon at the surface), export produc-
44 tion (related to the transport of organic material to depth) and the amount of remineralised carbon. On average, ESMs
45 project a decrease in globally averaged primary production and export production across various future scenarios of increas-
46 ing atmospheric CO₂ (Henson et al., 2022; Wilson et al., 2022; Kwiatkowski et al., 2020). Yet, these results differ region-
47 ally with, e.g., a general increase in the Arctic Ocean, Southern Ocean, and a general decrease in the equatorial Pacific
48 (~~?Henson et al., 2022; Wilson et al., 2022; Kwiatkowski et al., 2020~~)(Myksovoll et al., 2023; Henson et al., 2022; Wilson et al., 2022; Kwiatk
49 . Globally and regionally, the range of projected changes in primary production and export production differs largely between
50 ESMs such that the inter-model range of the change is often more than twice its multi-model mean (Tagliabue et al., 2021).
51 In contrast, more ~~rem mineralization~~rem mineralisation of organic matter in the interior can be expected due to a more sluggish
52 circulation (Tjiputra et al., 2018; Weijer et al., 2020), increasing the effectiveness of the BCP despite a reduced export produc-
53 tion from the surface (Liu et al., 2023). However, despite model consensus on a global increase of remineralised carbon across
54 scenarios, the amplitude varies widely between models (Wilson et al., 2022).

55 The quantity of remineralised carbon (DIC_{remin}) is a good indicator of the strength of the BCP and its impact on atmospheric
56 CO₂ (Marinov et al., 2008; Kwon et al., 2009; Koeve et al., 2020; Frenger et al., 2024). In a steady state climate, large DIC_{remin}
57 stocks correspond to low atmospheric CO₂ levels (Marinov et al., 2008; Frenger et al., 2024) and in a transient climate, the
58 strongest increase in DIC_{remin} corresponds to the strongest biologically-induced decline in atmospheric CO₂ (Koeve et al., 2020;
59 Frenger et al., 2024). In contrast, export production is unrelated to atmospheric CO₂ (Marinov et al., 2008; Kwon et al., 2009;
60 Frenger et al., 2024). DIC_{remin} can be estimated from apparent oxygen utilisation (AOU, Frenger et al. (2024); Wilson et al.
61 (2022)), which measures the deficit of oxygen compared to saturation. It is an estimate of the cumulative oxygen utilised to
62 remineralise organic material since the water parcel was last in contact with the atmosphere. Despite some limitations such as
63 assuming 100% oxygen saturation at the surface (Ito et al., 2004), changes in AOU can be used for quantifying the impact of
64 the BCP on atmospheric CO₂ (Koeve et al., 2020).

65 AOU is traditionally supposed to be the product of the oxygen utilisation rate (OUR) and an estimation of the time since the
66 water-mass was last in contact with atmosphere (Sulpis et al., 2023; Feely et al., 2004; Sarmiento et al., 1990). In regions

67 ~~with sufficient oxygen concentration~~dominated by advection or with an even spatial distribution of the respiration rate, the
68 relation between AOU and age is linear when ~~they-both~~ are affected similarly by transport (Koeve and Kähler, 2016). Typically
69 the linear relationship breaks in areas where gradients are too different (Thomas et al., 2020). A stronger ~~remineralization~~
70 remineralisation closer to the surface or below highly productive zones (e.g., equatorial Pacific) will locally increase AOU
71 without any correlation to a change in age. The linear relation between AOU and age has been used to estimate ~~the-OUR~~
72 (Sulpis et al., 2023) and as a proxy of water-mass age (Thomas et al., 2020). The relationship between trends or changes in
73 AOU and age can further be used to decompose changes in AOU into circulation-driven and biologically-driven factors. So far
74 this relationship has been little explored in future climate projection. Bopp et al. (2017) found a strong relationship in one ESM
75 from the Coupled Model Intercomparison Project Phase 5 (CMIP5), however, ventilation ages were not available for the other
76 CMIP5 models. More recently, Liu et al. (2023) explored the relation between changes in circulation and changes in AOU.
77 They found that the slowing down of the meridional overturning circulation, which is an indicator of ocean interior residence
78 time, would allow more time for the exported biogenic carbon to accumulate at depth and thus increase the deep ocean storage
79 of carbon by the BCP.

80 In this work we further explore the relationship between changes in circulation and changes in the BCP using Earth system
81 model simulations from the sixth Coupled Model Intercomparison Project (CMIP6) as well as observations from the Global
82 Ocean Data Analysis Project (GLODAPv2, Lauvset et al. (2024)). Following the approach suggested by Frenger et al. (2024),
83 we use remineralised DIC, ~~measured-estimated~~ from AOU, as indicator for the BCP. We show that changes in AOU are linearly
84 related to changes in age in large parts of the deep ocean. We further use the linear relationship to quantify the respective role
85 circulation changes play in the future evolution of the BCP. Lastly, we discuss future opportunities to constrain the estimates of
86 the deep ocean BCP with observations.

87 **Methods**

88 **2 Methods**

89 **~~Earth system models outputs and observational data~~**

90 **2.1 Earth system models outputs and observational data**

91 Eleven Earth system models (ESMs) provide the monthly 3D output fields required to compute AOU for the preindustrial
92 control (piControl), historical and SSP5-8.5 future scenario simulations in a replica of the CMIP6 database. Among these
93 eleven ESMs, only eight also provide outputs for the age tracer: MPI-ESM1.2-LR and MPI-ESM1.2-HR (Mauritsen et al.,
94 2019), ACCESS-ESM1.5 (Ziehn et al., 2020), IPSL-CM6A-LR (Boucher et al., 2020), MIROC-ES2L (Hajima et al., 2020),
95 NorESM2-LM and NorESM2-MM (Seland et al., 2020) and CanESM5 (Swart et al., 2019). We do not consider NorESM2-MM
96 and MPI-ESM1.2-HR here to keep only one variant of each model. We also do not consider CanESM5 because it does not
97 provide phosphate fields that are used to compute the PO-tracer (Broecker et al., 1991), required to define water-masses (see
98 ~~section about water masses definition~~subsection 2.3). Hence, five ESMs (Table 1) are selected to be ~~analyzed~~analysed in detail
99 in this work. For comparison, we also compute AOU for the four remaining ESMs (CanESM5, CNRM-ESM2-1 (Séférian
100 et al., 2019), GFDL-ESM4 (Dunne et al., 2020), UKESM1-0-LL (Sellar et al., 2020)).

101 To have an observational baseline over the recent period, we also conduct an observation-based analysis of the trends in AOU
102 and trends in age using ~~eo-located~~the observational data product GLODAPv2 (2016) (Key et al., 2015; Olsen et al., 2016). We
103 use temperature, salinity, phosphate and oxygen measurements~~as well as AOU and age estimates from the observational data~~
104 ~~product GLODAPv2.2024 (Lauvset et al., 2024)~~. AOU is computed in the same way as for the ESMs (~~see next section about~~
105 ~~AOU and remineralised carbon~~), while age is derived from subsection 2.2. We use the age product from Jeansson et al. (2021)
106 . In this product, measurements of the ~~chlorofluorocarbons (CFCs) CFC-11 and CFC-12, as well as the transient tracer sulphur~~

Table 1. The CMIP6 Earth system models analysed in this study, their ocean, sea-ice and marine biogeochemistry, and their ocean grid resolution

ESM	Ocean/sea-ice	Marine biogeochemistry	Ocean grid
ACCESS-ESM1-5 (Ziehn et al., 2020)	MOM5/CICE4	WOMBAT	1°, 50 vertical levels
IPSL-CM6A-LR (Boucher et al., 2020)	NEMOv3.6/LIM3	PISCESv2	1°, 75 vertical levels
MIROC-ES2L (Hajima et al., 2020)	COCO	OECO2	1°, 62 vertical levels
MPI-ESM1-2-LR (Mauritsen et al., 2019)	MPIOM1.6	HAMOCC6	1.5°, 40 vertical levels
NorESM2-LM (Seland et al., 2020)	BLOM/CICE5	iHAMOCC	1°, 70 vertical levels

107 ~~hexafluoride (SF6)(?)~~chlorofluorocarbon CFC-12 from GLODAPv2 (2016) are used with the transit time distribution (TTD)
 108 method to compute age, assuming 100 % saturation and a balance between advection and mixing, i.e. $\Delta/\Gamma = 1$. We only use data
 109 points where measurements of all variables mentioned are available. In order to be consistent with the age product, we opted for
 110 GLODAPv2 (2016), although more recent versions of the observational data product are available (e.g. Lauvset et al. (2024)
 111). The time range of the observational baseline is limited by the age dataset and extends from ~~1972–1982~~ to 2013. Only
 112 observations below 1000 metres ~~depth~~ are considered to avoid the influence of mixed-layer processes and subtropical gyres.

113 ~~Apparent oxygen utilisation and remineralised carbon~~

114 ~~2.2 Apparent oxygen utilisation and remineralised carbon~~

115 Apparent oxygen utilisation (AOU in $[\text{mol O}_2 \text{ m}^{-3}]$) is computed as:

$$116 \text{AOU} = O_2^{\text{sat}} - O_2 \quad \text{Equation 1.}$$

117 where O_2 is the in-situ dissolved oxygen concentration and O_2^{sat} is the dissolved oxygen concentration at saturation com-
 118 puted from temperature and salinity following Garcia and Gordon (1993, 1992). The amount of carbon resulting from this
 119 ~~remineralization~~ ~~remineralisation~~ ($\text{DIC}_{\text{remin}}$ in $[\text{g C m}^{-3}]$) is estimated as:

$$120 \text{DIC}_{\text{remin}} = m_C \times R_{\text{C:O}_2} \times \text{AOU} \quad \text{Equation 2.}$$

121 where m_C is the molecular weight of carbon (12.01 g mol^{-1}) and $R_{\text{C:O}_2}$ is the stoichiometric ratio between carbon and oxygen
 122 (117:170, Anderson and Sarmiento (1994)).

123 Although providing a reasonably good indication of the BCP strength and its impact on atmospheric CO_2 (Koeve et al., 2020;
 124 Frenger et al., 2024), AOU has a couple of pitfalls that should be kept in mind. First, it assumes that at the surface, oxygen
 125 concentration is in equilibrium with the atmosphere. This assumption is valid in most of the ocean, yet in high latitudes, water
 126 parcels can be detrained from the mixed layer while being under-saturated leading to an overestimation of respiration and
 127 AOU, notably in the deep ocean (Ito et al., 2004; Duteil et al., 2013). True Oxygen utilisation (Ito et al., 2004) or Evaluated
 128 Oxygen utilisation (Duteil et al., 2013) are intended to overcome this limitation. However, the computation of these variables
 129 requires additional tracers (e.g., preformed O_2 , (Tjiputra et al., 2020)) that are not routinely available in the CMIP6 output
 130 database. Another limitation is that AOU only measures aerobic ~~remineralization~~ ~~remineralisation~~. Yet, when oxygen levels
 131 are too low, anaerobic ~~remineralization~~ ~~remineralisation~~ will take place and use other oxidants (e.g., nitrate for denitrification)
 132 instead of oxygen. In the open ocean, denitrification typically occurs in suboxic waters, when oxygen concentrations drop
 133 below $5 \mu\text{mol O}_2 \text{ l}^{-1}$ (Keeling et al., 2010). Suboxic waters represent only 0.1% of the contemporary ocean and are located in
 134 the upper 1000 metres (Deutsch et al., 2011; Keeling et al., 2010). During the 21st century, suboxic volume may extend but is
 135 projected to not exceed 1% of the ocean volume (Deutsch et al., 2011; Cocco et al., 2013; Fu et al., 2018).

Water-masses definition

2.3 Definition of water-masses

We aim to find a linear relationship between the spatial distribution of AOU trends and age trends that is representative for most of the deep ocean. From now on and unless specified otherwise, we define the deep ocean as the ocean below 1000 metres. We assess the linear relationship within different water-masses of the deep ocean characterized with a combination of the PO-tracer (PO^* , Broecker et al. (1991)) and density.

For the water-mass definition of the ESMs, neither density nor PO^* are standard outputs in the CMIP6 database so that we compute density with the Gibbs SeaWater (GSW) Oceanographic Toolbox of TEOS-10 in xarray (Caneill and Barna, 2024; McDougall and Barker, 2011) and PO^* based on the definition by Broecker et al. (1991) ($PO^* = PO_4 + O_2/175$). Both variables are averaged over the years 1972–1982 to 2013, i.e., the time period covered by the observational dataset used in this work. Our water-mass definition for the ESMs focuses only on the deep ocean below 1000 metres and uses PO^* -thresholds to define water-masses originating in the North Atlantic and Southern Ocean (respectively $0.35 < PO^* \leq 0.91$ and $0.91 < PO^* \leq 2$). These thresholds are derived from Broecker et al. (1998), yet they have been refined by iterative testing to better suit the ESMs. Only Broecker et al. (1998) state that the global distribution of PO^* has its minimum in the North Atlantic, its maximum in Southern Ocean and that the PO^* distribution for deep waters formed in the North Atlantic is very distinct from the distribution for deep waters formed in the Southern Ocean. Based on these statements, we defined PO^* -thresholds for deep ocean water masses individually for each ESM, using PO^* averaged on 1982–2013 and applying the following approach: (i) We compute the 95th percentile of the PO^* distribution in the deep subpolar North Atlantic, between $40\text{--}60^\circ\text{N}$ and $0\text{--}70^\circ\text{E}$. (ii) We compute the 5th percentile of the PO^* distribution in the deep Southern Ocean, south of 55°S . (iii) The PO^* -threshold is defined as the average between the aforementioned percentiles. We find that Atlantic water-masses have PO^* values below the threshold while Southern water-masses have PO^* values above the threshold (see supplementary Fig. S1). For the Southern water-masses, it is necessary to exclude grid-cells located south of 60°N and to exclude grid-cells in the Arctic Ocean, as some Arctic Ocean grid-cells would otherwise be included without being continuously connected to the Southern Ocean. All longitudes are considered for the Southern water-masses. For the Atlantic water-masses, only grid-cells located between 90°E east of the Drake passage, west of 30°E and south of 80°N are included to exclude grid-cells in the Pacific and Indian Oceans that fulfill the PO^* -threshold. Each of these and to exclude grid-cells in the Arctic Ocean. In the Arctic Ocean, a linear relationship between AOU trends and age trends emerges but with a very different slope than the one found for the Atlantic water-masses: here, AOU trends seem to be much more sensitive to age trends (not shown). Since our focus is on identifying linear relationships representative for most of the deep global ocean, we decided to exclude the Arctic from the analysis. We split the Southern and Northern water masses into half according to density (see supplementary Tab. supplementary Table S1), leading to four water-masses: (i) the Atlantic light waters, (ii) the Atlantic dense waters, (iii) the Southern light waters, and (iv) the Southern dense waters. These four water-masses cover between and at least 70 % of the entire deep ocean, depending on the ESM (70 % for IPSL-CM6A-LR and at least 92 % for the other models). For each water-mass and each ESM we define a spatial mask (supplementary Fig. S2), which is used to identify grid points belonging to the same water-mass and compute the linear regression between trends in AOU and trends in age (see next section subsection 2.4). We keep the masks constant throughout the historical and SSP5-8.5 simulations as the masks show minimal sensitivity to the time period used for creating the PO^* and density fields (supplementary Figs. S2 and S3).

Similar to the definition of water-masses used for the ESMs, observations/observational data points are classified into water masses originating in water-masses originating from the Southern Ocean and North Atlantic (supplementary Fig. S4) based on their PO^* values (supplementary Fig. ??). Waters originating in the Southern Ocean are defined via $1.2 \leq PO^* \leq 2.0$ $\mu\text{mol PO}_4 \text{ kg}^{-1}$ and those originating in the North Atlantic Ocean via $PO^* < 1.2$ $\mu\text{mol PO}_4 \text{ kg}^{-1}$ with PO^* thresholds based on Broecker et al. (1998). In lighter density classes, due to the fanning out of temperature and salinity, the number of data is too low to identify a relationship between AOU trends and age trends. Thus, the resulting water-masses are already relatively dense, with an average of $\sigma_0 = 27.7 \text{ kg m}^{-3}$ and density no lighter than and were. Most of the data points used in this

work belong to the densest half of waters originating from the North Atlantic Ocean or the Southern Ocean (98 % and 75 % of the points respectively). They were therefore not further separated into light and dense waters. The water-masses will be referred to as Southern dense waters and North Atlantic dense waters to facilitate a meaningful comparison with their model counterparts and are most representative of the water-mass end members.

Relationship between trends in AOU and trends in age

2.4 Relationship between trends in AOU and trends in age

Just as the relationship between AOU and age can be linear (Sulpis et al., 2023), one might expect that the trends in AOU and the trends in age can be linearly related. In this work we intend to express the trends in AOU ($\frac{d\text{AOU}}{dt}$) via trends in age ($\frac{d\text{age}}{dt}$), in each point X , as follows:

$$\frac{d\text{AOU}}{dt}(X) = S_{\Delta\text{Age}}^{\Delta\text{AOU}} \times \frac{d\text{age}}{dt}(X) + B + \varepsilon(X). \quad \text{Equation 3.}$$

We assess the linear relationship between spatial fields of AOU trends and age trends within the previously define water-masses using a linear regression (Virtanen et al., 2020). The slope of the linear regression is the sensitivity of AOU changes to age changes ($S_{\Delta\text{Age}}^{\Delta\text{AOU}}$), the intercept is B and ε represents a spatial average of the changes in AOU when there is no change in age. $\varepsilon(X)$ is the error of the linear regression in each point. All together, $B + \varepsilon$ gathers changes represents the change in AOU that are not linearly related to changes in ages such as changes in remineralization, e.g. changes in remineralisation rates. $S_{\Delta\text{Age}}^{\Delta\text{AOU}}$ defined here is connected to the oxygen utilisation rate (OUR) defined in other studies (Sulpis et al., 2023; Feely et al., 2004). Indeed, if the equation $\text{AOU} = \text{OUR} \times \text{age}$ is differentiated with respect to time, then $S_{\Delta\text{Age}}^{\Delta\text{AOU}}$ and OUR are a similar quantity: an estimate of a spatio-temporal average of the local instantaneous oxygen utilisation rate. We choose to call the slope of the linear regression $S_{\Delta\text{Age}}^{\Delta\text{AOU}}$ instead of OUR for two reasons: 1) we think this word convey conveys more accurately the purpose of the analysis, i.e. investigating the relationship between AOU trends and age trends and 2) we want to avoid ambiguity with studies working at estimating OUR (e.g. Sulpis et al. (2023); Sulpis et al. (2023); Guo et al. (2023); Jenkins (1982)).

For the analysis of the ESMs, it is crucial to estimate and remove the drifts in the simulated fields of AOU and age tracer before calculating their respective trends. The trends and drifts are estimated for every ocean grid-cell of the ESMs using a linear regression over years 1850 to 2099 250 years of the piControl simulation (note that actual years are adjusted to fit 1850-2099, see supplementary Tab., starting from the year in the piControl simulation where the historical simulation has been initialised (supplementary Table S2). Outputs from the historical and SSP5-8.5 simulations are then drift corrected for each point in time t ($X_{\text{drift-corrected}}(t) = X_{\text{drift-uncorrected}}(t) - (t - t_0) \times \text{drift}$, with t_0 referring to 1850) before computing the trends. The trends are computed for using a linear regression over the years (i) 1972-2013-1982-2013 of the historical simulation to match the time period of available observational data and (ii) 2015-2099 (the entire SSP5-8.5 simulation). When considering the ESMs, for the time period 1972-2013-1982-2013, between 49 % (NorESM2-LM) and 72 % (IPSL-CM6A-LR, MIROC-ES2L) of the deep ocean grid points have significant trends (p-value ≤ 0.05) in both AOU and age, while between 84 % (NorESM2-LM) and 94 % (MIROC-ES2L) have significant trends for the time-period 2015-2099 (see supplementary Fig. S5). The non-significant trends are very close to zero. For each ESM, we only consider grid-points with significant trends for computing the linear regression in each water-mass.

To overcome the difficulty of identifying trends with highly spatio-temporally sparse observational data, as it is the case for age estimates, we collapse the available observations in Temperature-Salinity temperature-salinity (T-S) space. Trends in AOU and age are computed within bins in the T-S space (supplementary Fig. S6). Temperature ranges between 1.5 and 8 and is divided into 350 bins while salinity ranges between 34.2 and 34.9 and is divided into 300 bins. The chosen resolution of the T-S bins, about and, comes from the trade-off between To ensure that data points are geographically close to each other within each T-S bin, we (i) remove outliers defined as data points geographically further than twice the median distance to the median location and (ii) only keep points that are within a maximum distance from the median location (recomputed without the outliers). Thus

222 ~~the computation of the trends depends on two choices: the temperature and salinity resolution for the T-S bins and the maximum~~
223 ~~distance from the median location within each T-S bins. These choices affect: (i) ensuring that comparable measurements are~~
224 ~~grouped the grouping of comparable measurements into the same T-S bin even if they have a different T-S bin, regardless of~~
225 ~~their geographical location, (ii) providing enough the number of data points per T-S bins to find significant T-S bin needed~~
226 ~~to identify significant trends (p-value ≤ 0.05) trends, and (iii) providing enough trends the number of trend estimates (one~~
227 ~~per T-S bins) to identify T-S bin required to establish a significant (p-value ≤ 0.05) relationship correlation between AOU~~
228 ~~trends and age trends. Trends for AOU and age, (dAOU/dt) and (dage/dt) are computed when five or more observations are~~
229 ~~grouped into a given T-S bin. Trends are then grouped into the Southern and Atlantic water-masses defined previously. For the~~
230 ~~Southern water-mass, out of 1076 trends identified, 77 are significant for age and 107 for AOU. For the Atlantic water-mass,~~
231 ~~1816 trends are identified, out of which 188 are significant for age and 246 for AOU. When accounting only for the co-located~~
232 ~~measurements that have significant trends both in age and AOU, Due to the substantial influence of the number of trends is~~
233 ~~reduced to 23 and 118 for T-S bin size and the maximum distance, we conduct the analysis of the observational data 625 times~~
234 ~~with different random choices of these parameters to derive a distribution of the observation-based $S_{\Delta \text{Age}}^{\Delta \text{AOU}}$. Temperature/salinity~~
235 ~~resolutions ranged from 0.026 °C to 0.325 °C and 0.0024 to 0.03, while maximum distance from 500 km to 5000 km. Trends~~
236 ~~are then grouped into the Southern and Atlantic water-masses, respectively. As in the modeling defined previously. Finally,~~
237 ~~as in the modelling counterpart of the analysis, a linear regression was is computed between the spatial distributions of AOU~~
238 ~~trends and the age trends, which is then used as an observational constraint.~~

239 In this work we apply linear regressions for estimating trends and evaluating linear relationships. ~~In these applications~~ Further,
240 we evaluate the significance of the trends and the linear relationship base on the p-values testing the null hypothesis of zero
241 slopes, i.e. no trends or no linear relationship. When the p-value is lower than or equal to 0.05 we consider the trends or the
242 linear relationship to be significant. The linear regression also provides a 95 % confidence interval for the slope, serving as a
243 measure of the uncertainty associated with $S_{\Delta \text{Age}}^{\Delta \text{AOU}}$. If this uncertainty is not specifically stated, it means that it is negligible with
244 respect to the number of significant figures provided.

245 2.5 Evaluation of model-observation comparability

246 The analytical approach applied to observational data differs from the one applied to model outputs in three ways. (1) For the
247 observational data, age is estimated using the TTD method with measurements of CFC-12. This method compares measured
248 CFC-12 concentrations in the ocean with the evolution of CFC-12 concentrations in the atmosphere, assuming some balance
249 between mixing and advection in ocean circulation. However, ESMs calculate the age via the tracer ideal-age, which is carried
250 by the simulated ocean circulation and ageing at a rate of one year per year once it has left the ocean surface. Hereafter, where
251 necessary, we will distinguish between "ideal-age" and "TTD-mean-age", the latter referring to age estimates derived from
252 CFC-12. Where no distinction between the two is necessary, we will simply refer to "age". (2) Observational datasets suffer
253 from sparse and heterogeneous sampling in space and time, whereas ESM model results cover the entire ocean on a regular
254 grid with monthly frequency. (3) Because the number of observational data is limited, trends must be computed within T-S bins
255 while the outputs from ESMs gives time series for each grid-point.

256 We quantify the uncertainties in $S_{\Delta \text{Age}}^{\Delta \text{AOU}}$ estimates derived from the observational dataset related to the aforementioned limitations
257 using outputs from the NorESM2-LM historical simulation. We run two analysis:

- 258 • In TTD-UNC we quantify the uncertainties related to using the TTD method. To do so, we applied the TTD method
259 to CFC-12 outputs from NorESM2-LM. Then, similar to the analysis of the ESMs ensemble (section 2.4), (i) we
260 compute trends in TTD-mean-age, (ii) we identify a linear relationship between the spatial fields of AOU trends and
261 TTD-mean-age trends in the Atlantic dense and Southern dense water-masses and (iii) we derive $S_{\Delta \text{Age}}^{\Delta \text{AOU}}$ values. In
262 NorESM2-LM simulations, CFC-12 only partially invaded the ocean; e.g. most of the Pacific and Indian Oceans north
263 of 40°S have CFC-12 concentration too small to derive a TTD-mean-age. Thus, in this analysis, we also sample the

ideal-age outputs based on the spatio-temporal distribution of TTD-mean-age and derive reference values of $S_{\Delta\text{age}}^{\Delta\text{AOU}}$ using this ideal-age sample for the Atlantic dense and Southern dense water-masses. $S_{\Delta\text{age}}^{\Delta\text{AOU}}$ values derived from TTD-mean-age is compared against the reference $S_{\Delta\text{age}}^{\Delta\text{AOU}}$ values derived from ideal-age to quantify the uncertainty due to the TTD method.

- In SAMPLE-UNC, we quantify uncertainties due to data scarcity and the necessity to compute trends in T-S bins. We sample in space and time the NorESM2-LM outputs based on the observational data and replicate the analysis applied to the observational datasets, i.e. trends computed in T-S bins with the same 625 choices for T-S bins sizes and maximum distance that were used for the analysis of the observational dataset. The comparison between the obtained distribution of $S_{\Delta\text{age}}^{\Delta\text{AOU}}$ and the original $S_{\Delta\text{age}}^{\Delta\text{AOU}}$ values (no sampling, trends computed in each grid-point) quantifies the uncertainty of the T-S bins approach as well as of the data scarcity.

Results

3 Results

3.1 Contemporary and future AOU across Earth system models

Contemporary spatial AOU patterns reflect physical transport and biological oxygen consumption. For example, AOU is particularly high in areas combining weak ventilation or ventilation of oxygen-depleted water-masses and intense remineralization remineralisation such as the deep ocean, the North Pacific or in the upper 1000 metres in the equatorial band (Fig. 1a,b,c). Earth system models (ESMs) reproduce the general patterns shown by observations-gap-filled observational products from the World Ocean Atlas 2023 (supplementary Fig. S7), yet with some regional strong positive and negative biases relative to observations (Fig. 1d,e,f). On average, ESMs overestimate AOU in the ocean deeper than 2000 metres north of ca. 40°S and below 1000 metres in the Pacific north of ca. 50°S. In contrast, ESMs underestimate AOU in the Southern Ocean (south of ca. 30°S) and above 1000 metres depth-in-the-whole-in-the northern hemisphere. In addition to these-biases in the model-mean, we note that there is a strong inter-model spread in large parts of the ocean, where the range of ESM values is higher than 70 % of the observation value (stippling in Fig. 1d,e,f and supplementary Fig. S8).

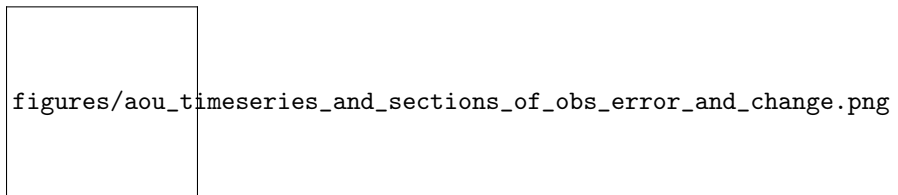


Figure 1. Evaluation of apparent-oxygen-utilisation-(the-simulated AOU) and consistency in the projected future-change (ΔAOU) as-simulated-by-Earth-system models-(ESMs). (a, b, c) AOU from the World Ocean Atlas 2023 (WOA23, Garcia et al. (2024)), averaged over 1971-2000 in the Atlantic (10°W to 60°W), Pacific (130°W to 180°W) and Indian (40°E to 90°E) sectors of-the-ocean. (d, e, f) Multi-model mean of AOU bias against WOA23. Stippling shows AOU uncertainty in ESMs, i.e. when the range between the highest and lowest ESM values is greater than 70 % of the WOA23 value. Refer to supplementary Fig. S8 for individual ESM bias. (g, h, i) Multi-model mean of projected change (1971-2000 minus 2070-2099) under the SSP5-8.5 scenario, zonally average. Stippling shows ΔAOU uncertainty in ESMs, i.e. when the range between the strongest and weakest ΔAOU exceed three times the multi-model mean ΔAOU . Refer to supplementary Fig. S9 for individual ESM ΔAOU . The red dashed lines indicate the 1000 metres depth-separating the upper and deep ocean. (j, k, l) Time series of ΔAOU integrated on the (j) global, (k) upper and (l) deep ocean for each ESM considered in this study. The gray shading shows the range of other ESMs not used in this study (CanESM5, CNRM-ESM2-1, GFDL-ESM4, UKESM1-0-LL). The vertical dashed gray line (year 2015) separates the historical and SSP5-8.5 scenarios.

In the majority of the ocean, AOU is projected to increase under the SSP5-8.5 scenario (Fig. 1g,h,i). Most of the increase occurs below 1000 metres (Fig. 1l), with agreement on the sign of change among the models (supplementary Fig. S9). Above 1000 metres, AOU is projected to decrease in areas around the Equator or near the surface in the high latitude (Fig. 1g,h,i). The uncertainty of the projected change is considerable between ESMs with the inter-model spread exceeding three times the

291 multi-model mean in the intermediate depth of the Pacific, in the low-latitude Indian, and in the deep subtropical North Atlantic
292 (stippling in Fig. 1g,h,i and supplementary Fig. S9). By 2099, the integrated projected global change in AOU compared to 1850
293 ranges from 20 to 76 PgC (Fig. 1j). A substantial share of the inter-model uncertainty in AOU changes stems from the deep
294 ocean (below 1000 metres). Here, the ESM spread encompasses 20 to 65 PgC (Fig. 1l), while it ranges from -10 to 25 PgC
295 above 1000 metres (Fig. 1k). The inter-model differences in AOU changes within the ESMs used in this study is representative
296 of the inter-model differences in the AOU changes as seen by other ESMs (grey shading in Fig. 1j,k,l).

297 3.2 $S_{\Delta \text{age}}^{\text{AAOU}}$ across Earth system models

298 For our model ensemble and the grid-points with significant trends in AOU and age-ideal-age in our defined Atlantic and
299 Southern water-masses, the AOU trends are significantly correlated with the age-ideal-age trends for the years 1972-2013
300 1982-2013 (Fig. 2 and supplementary Fig. S10) and 2015-2099 (supplementary Fig. S11). ~~The coefficient of determination,~~
301 ~~R^2 , is higher than 0.7, indicating that the~~ In at least four out of five ESMs, spatial variability in age-ideal-age trends can explain
302 more than half of the spatial variability in AOU trends, ~~for four out of five ESMs in the dense~~ in all four water-masses ~~and~~
303 ~~three out of five ESMs in the light water-masses. We only find weaker correlations between AOU trends and age trends in~~
304 ~~five cases (see $R^2 < 0.7$ in Fig. 2). This is probably related to the definition of the different~~ for the contemporary period, i.e.
305 the coefficient of determination R^2 is higher than 0.5. Weaker correlations are potentially related to significant contribution of
306 mixing over advection, spatial variability or local changes of respiration rate, or a partially inappropriate definition of
307 water-masses ~~not being fully appropriate for all models. For example, some deep grid points counted towards the~~ in MPI-ESM1.2-LR,
308 some of the grid-points included in the Atlantic light waters could arguably be included in the Atlantic dense waters. ~~In addition,~~
309 ~~some of the grid-points defined as light waters are situated around 1000 metres and could be part of sub-surface waters such~~
310 ~~as the Antarctic Intermediate Waters or Subantarctic Mode Water. Indeed, these grid points have densities very close to the~~
311 median, their depths are comparable to those of Atlantic dense waters and they exhibit a linear relationship more similar to the
312 one in Atlantic dense waters. For IPSL-CM6A-LR, in some grid-points of the Atlantic dense waters ideal-age unexpectedly
313 increases while AOU decreases. These grid points, located in the Nordic Seas at approximately 3000 meters depth, may have a
314 different history compared to other Atlantic waters and thus would require a separate definition for their water mass. The linear
315 regression analysis cover only between and In most ESMs, the correlation between AOU and ideal-age trends is weaker in the
316 future period for all water-masses except the Southern dense waters, as indicated by the red vertical dashes in Fig. 3 (refer also
317 to supplementary Fig. S14). Hence, ideal-age contributes less to the spatial variability of AOU. Depending on the ESM, our
318 analysis covers only between 43 % and 66 % of the deep ocean for the ~~1972-2013 period, depending on the ESM,~~ 1982-2013
319 period, because i) we only consider grid points with significant trends in age-ideal-age and AOU, and ii) large part of the deep
320 ocean have weak and non-significant trends during the contemporary period. For the 2015-2099 period, the linear regression
321 analysis ~~cover between and~~ covers between 65 % and 94 % of the deep ocean, ~~depending on the ESM,~~ as the trends are stronger
322 and more significant (supplementary Fig. S11 and Fig. S5). The inclusion of the non-significant trends decreases R^2 but
323 does not substantially alter the slope of the linear regression (supplementary Fig. S12 and Fig. S13). ~~A positive linear~~
324 ~~correlation is also found between the significant trends in AOU and age from the observation dataset (supplementary Fig.~~
325 ~~??). Here, R^2 is 0.88 and 0.92 for the Southern and Atlantic water-masses, respectively, suggesting that about of the spatial~~
326 ~~variability in AOU trends can be explained by the spatial variability in age trends for the few significant trends in the Southern~~
327 ~~and Atlantic water-masses.~~

260114_REVISION1/figures/scatter_plot_aou_trend_vs_age_trend_historical_1982-2013_signif.png

Figure 2. Distribution of the trends in age-ideal-age and trends in apparent oxygen utilisation (AOU) for the contemporary period (1972-20131982-2013) simulated with five Earth system models (ESMs): a) MPI-ESM1.2-LR, b) ACCESS-ESM1.5, c) IPSL-CM6A-LR, d) MIROC-ES2L, e) NorESM2-LM. The blue shading shows the number of data point for each bin of age-ideal-age trends and AOU trends for the Southern and Atlantic light/dense waters, accounting only for grid-points where ideal-age and AOU trends are significant. A linear regression is computed between the AOU trends and age-ideal-age trends for each water-mass. On each panel, the slope ($S_{\Delta\text{age}}^{\Delta\text{AOU}}$), the coefficient of determination (R^2) and the fraction of the deep ocean volume are shown in different colours for each water-massewater-masse. The gray shading show the distribution of trends for the entire ocean.

328 The simulated sensitivities of AOU change to age-ideal-age change ($S_{\Delta\text{age}}^{\Delta\text{AOU}}$) are relatively similar in the for both light and dense
329 waters. Yet, as might be expected, given that remineralization is stronger in the shallower regions, $S_{\Delta\text{age}}^{\Delta\text{AOU}}$ is slightly stronger
330 in light waters, likely due to stronger remineralisation in the shallower regions. We find that ESMs with a large (small) $S_{\Delta\text{age}}^{\Delta\text{AOU}}$
331 in the contemporary period (1972-20131982-2013) also have a large (small) $S_{\Delta\text{age}}^{\Delta\text{AOU}}$ for the future period under the high CO₂
332 future scenario SSP5-8.5 climate change scenario (Fig. 3). In addition, for each ESM, the future $S_{\Delta\text{age}}^{\Delta\text{AOU}}$ is similar or smaller
333 than the contemporary one (except for three cases, points above the 1:1 line in Fig. Fig. 3), suggesting a reduction of the
334 remineralization rate under the SSP5-8.5 climate change scenario. The linear relation between present and future $S_{\Delta\text{age}}^{\Delta\text{AOU}}$ is
335 strong for the Southern light and dense waters and the Atlantic dense waters across our model ensemble, as indicated by
336 a the linear regression giving coefficients of determination higher than 0.70.97 and p-values below 0.050.01 (Fig. 3). The only
337 exception are the Atlantic light waters with a weak linear relation across the model ensemble, mainly In the Atlantic waters,
338 the linear relationship is not significant (p-value > 0.05), mostly due to the behavior of NorESM2-LM. $S_{\Delta\text{age}}^{\Delta\text{AOU}}$ evaluated from
339 the observations are for the Atlantic dense and Southern dense water masses, respectively (vertical blue line and shading in
340 Fig. 3). They have not been split into light and dense waters due to the limited number of data points (see methods). In both
341 cases, the values are on the low side of the ESMs range: 0.08 to 0.29 and 0.06 to 0.18 for the distinct behaviour of two models.
342 Specifically, $S_{\Delta\text{age}}^{\Delta\text{AOU}}$ in NorESM2-LM does not decline in the future period for Atlantic dense and Southern dense water masses,
343 respectively light waters, and $S_{\Delta\text{age}}^{\Delta\text{AOU}}$ in MIROC-ES2L shows a substantial decrease in the future period for Atlantic dense waters.

figures/constraint_plot_linreg Δ AOUvs Δ Age_in_SSP585_vs_linreg Δ

Figure 3. Distribution of the sensitivity of AOU change to age-ideal-age change ($S_{\Delta\text{Age}}^{\Delta\text{AOU}}$) in each water-masse water-mass: a) Southern light, b) Atlantic light, c) Southern dense, and d) Atlantic dense. Each dot shows the $S_{\Delta\text{Age}}^{\Delta\text{AOU}}$ for one Earth system model (ESM) on the contemporary (1972-2013) and future (2015-2099) period. For few models, the red horizontal/vertical dash indicates a weak correlation ($R^2 < 0.7$) between AOU trends and age-ideal-age trends for the contemporary/future period. The black line shows the linear regression and the gray shading its confidence interval. The associated coefficient of determination (R^2) and the p-value are indicated in each panel. The diagonal dashed gray line is the 1:1 line. The vertical blue lines (and shading) show the $S_{\Delta\text{Age}}^{\Delta\text{AOU}}$ (and its uncertainty) on years 1972-2013 estimated from observations of the GLODAPv2 database, only for the Southern and Atlantic dense water-masses.

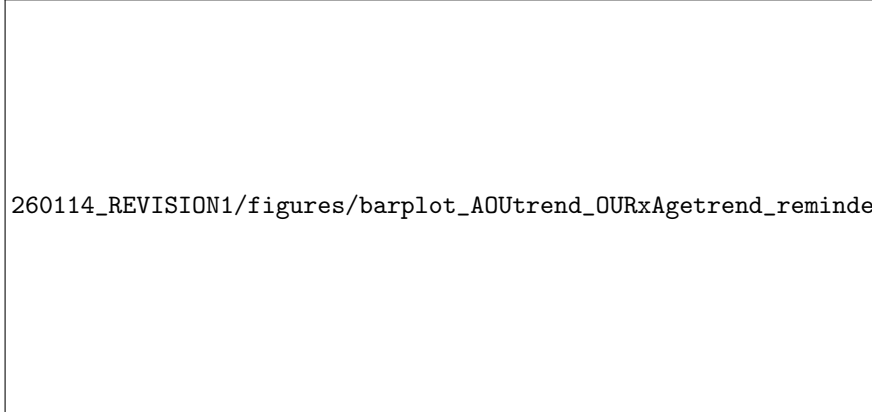
344 Once a linear relationship has been established providing the average trend in AOU for a given trend in age-ideal-age, we can use
345 it to further quantify the contribution of age-ideal-age trends to the trends in AOU in each ESM. This contribution is estimated by
346 multiplying the age-trends by $S_{\Delta\text{Age}}^{\Delta\text{AOU}}$ estimated in ideal-age trends with $S_{\Delta\text{Age}}^{\Delta\text{AOU}}$ for each of the four water-masses ($S_{\Delta\text{Age}}^{\Delta\text{AOU}} \times \frac{\text{dage}}{\text{dt}}$
347 in Eq. 3). Globally integrated, age-trends contribute from ideal-age trends contribute between 43 % (ACCESSM-ESM1.5) to
348 and 106 % (IPSL-CM6A-LR) of to the AOU trends in these water-masses (Fig. ??a4). In general, the positive trends in AOU
349 mostly arise from the Southern dense water-mass, and are driven by positive trends in age-ideal-age (Fig. ??b-p5). The Atlantic
350 dense water-mass exhibits also intense local positive AOU trends driven by age-ideal-age trends. In these two ventilation
351 regions, the models suggest a weakening in the ventilation rates in the future (increasing age-ideal-age). In contrast, negative
352 AOU trends are mostly located in the Southern and Atlantic light water-masses, found between 1000 and 2000 metres depth
353 in the subtropics and equatorial region. In these areas, negative age-ideal-age trends play a major role indicating that waters
354 get younger because of a shift in water-mass structure or stronger ventilation, thought though stronger ventilation seems less
355 likely considering that stratification increase everywhere in the ocean in the future simulation (Kwiatkowski et al., 2020). Such
356 distinction between light and dense water-masses have been previously identified for the contemporary period in the Nordic
357 Seas (Jeansson et al., 2023). The remainder term, $B + \varepsilon$, locally either slightly compensates or reinforces changes driven by age
358 trends ideal-age trends, resulting globally in a positive contribution to AOU trends. MPI-ESM1.2-LR, the ESM with the lowest
359 $S_{\Delta\text{Age}}^{\Delta\text{AOU}}$ and closest to the observation estimate, has a water-mass averaged coefficient of determination, $\overline{R^2}$, of 0.78 and estimate
360 the contribution of age-trends to (Fig. ??a). MIROC-ES2L and NorESM2-LM, whose $S_{\Delta\text{Age}}^{\Delta\text{AOU}}$ is also relatively close to the
361 observation estimate for at least one of the water-masses, have higher contribution of age trends. However, $\overline{R^2}$ is below 0.7 for
362 these two models. MPI-ESM1.2-LR and MIROC-ES2L are quite contrasted in terms of global trends in AOU and contribution
363 from age trends. In addition, MPI-ESM1.2-LR simulates strong AOU trends, driven by age trends, in the Atlantic dense waters
364 north of 50, between 2000 and 3000 metres depth, a feature not present in MIROC-ES2L (Fig. ??b,ck,l). The significant trends
365 in the four water-masses cover at least of the deep ocean. Integrated over these water-masses, the AOU trends are very close to
366 AOU trends integrated on the entire deep ocean (dark grey bars versus black contour bars in Fig. ??a) and represent a significant
367 part of the globally integrated AOU trends (dark grey bars versus light grey bars in Fig. ??a).

368 Discussion and conclusions

369 Understanding changes in ocean BCP and its impact on future climate change remains an outstanding research question
370 (Tjiputra et al., 2025). In this work, we have demonstrated that the spatial fields of AOU trends (an indicator of BCP) and
371 age trends are strongly correlated in the ocean deeper than 1000 metres where spatial variability in age trends can explain at
372 least of the spatial variability in AOU trends ($R^2 \geq 0.7$). This relationship is identified in simulations of the contemporary
373 period (1972-2013).

374 3.3 $S_{\Delta\text{Age}}^{\Delta\text{AOU}}$ from observational data

Trend in apparent oxygen utilisation ($\frac{d\text{AOU}}{dt}$) and the contribution from trends in age ($S_{\Delta\text{Age}}^{\Delta\text{AOU}} \times \frac{d\text{age}}{dt}$) under the SSP5-8.5 climate change scenario simulated with five Earth system models (ESMs): MPI-ESM1.2-LR, ACCESS-ESM1.5, IPSL-CM6A-LR, MIROC-ES2L, NorESM2-LM. The remainder ($B + \epsilon$) is computed as the difference between the two aforementioned components (see Eq. 3). Panel a) shows the trends spatially integrated over the global ocean (light grey), the deep ocean (black contour) and the four water-masses considered in this study (dark grey, dark blue and light pink). The white percentage in the dark blue bars indicates the share of the age-trends contribution to AOU-trends integrated on the four water-masses. At the bottom of the panel, 'Vol. ratio' indicates the share of the deep ocean volume covered by the four water masses, while $\overline{R^2}$ indicates the volume-weighted average of the coefficient of determination over the four water masses. Panels b-p) shows the zonally average trends for each ESM (in rows): first column displays $\frac{d\text{AOU}}{dt}$, the second column $S_{\Delta\text{Age}}^{\Delta\text{AOU}} \times \frac{d\text{age}}{dt}$ and the third one the remainder $B + \epsilon$. Trends are computed for the period from 2015 to 2099.



260114_REVISION1/figures/barplot_AOUtrend_OURxAge trend_reminder_global_integral.png

Figure 4. Spatially integrated trend in apparent oxygen utilisation ($\frac{d\text{AOU}}{dt}$, dark and light grey) and the contribution from trends in ideal-age ($S_{\Delta\text{Age, darkblue}}^{\Delta\text{AOU}} \times \frac{d\text{age}}{dt}$) under the SSP5-8.5 climate change scenario simulated with five Earth system models (ESMs): MPI-ESM1.2-LR, ACCESS-ESM1.5, IPSL-CM6A-LR, MIROC-ES2L, NorESM2-LM. The remainder ($B + \epsilon$, pink) is computed as the difference between the two aforementioned components (see Eq. 3). Shown are the trends integrated over the global ocean (light grey), and over the water-masses considered in this study. Trends are computed for the period from 2015 to 2099.

A positive linear correlation is also found between the significant trends in AOU and TTD-mean-age from the observation dataset (supplementary Fig. S15). $S_{\Delta\text{Age}}^{\Delta\text{AOU}}$ evaluated from the observational dataset are 0.04 ± 0.04 and 0.05 ± 0.01 $\text{mmol O}_2 \text{ m}^{-3} \text{ yr}^{-1}$ for the Southern dense and Atlantic dense water-masses, respectively (supplementary Fig. S15). Here, the water-masses have not been split into light and dense waters due to the limited number of data points (see subsection 2.3). For both water-masses, the coefficient of determination, R^2 , varies between 0.2 and simulations of the future period (2015-2099) under the SSP5-8.5 climate change scenario. The sensitivity of AOU change to age change, $S_{\Delta\text{Age}}^{\Delta\text{AOU}}$ (that is, the slope of the linear regression), varies between the ESMs and the water masses from 0.06 to 0.34 for the contemporary period, when considering only the linear relationship associated with $R^2 \geq 0.7$. $S_{\Delta\text{Age}}^{\Delta\text{AOU}}$ remain relatively similar when computed for the 2015-2099 period. Using the linear relationship we estimate that, on the 2015-2099 time period, the increase in age due to changes in circulation or ventilation rates contribute between and to the increase in deep ocean $\text{DIC}_{\text{rem}}^{\text{rem}}$ depending on the ESM. 1 depending on the methodological choices for the analysis, with higher R^2 values typically associated with higher $S_{\Delta\text{Age}}^{\Delta\text{AOU}}$.

Our estimates of $S_{\Delta\text{Age}}^{\Delta\text{AOU}}$

The scarcity of observational data and the use of the TTD-mean-age introduce uncertainties into the observation-based $S_{\Delta\text{Age}}^{\Delta\text{AOU}}$. When the analysis is replicated with a sample of NorESM2-LM outputs (SAMPLE-UNC analysis, see subsection 2.5), $S_{\Delta\text{Age}}^{\Delta\text{AOU}}$ estimates are 0.17 ± 0.04 and 0.18 ± 0.04 $\text{mmol O}_2 \text{ m}^{-3} \text{ yr}^{-1}$, for the Southern dense and Atlantic dense water-masses, respectively (Table 2). This is an increase of 0.08 and 0.04 $\text{mmol O}_2 \text{ m}^{-3} \text{ yr}^{-1}$ when compared to the reference values (analysis with non-scarce data). Using trends in TTD-mean-age as an estimate of trends in age introduce further uncertainties in the estimate of $S_{\Delta\text{Age}}^{\Delta\text{AOU}}$ from the observational dataset (TTD-UNC analysis, see subsection 2.5). When computed with CFC-12 outputs from NorESM2-LM, trends in TTD-mean-age are generally much stronger than trends in ideal-age (not shown). In some

Table 2. Sensitivity of AOU trends to age trends ($S_{\Delta\text{age}}^{\Delta\text{AOU}}$ in $\text{mmolO}_2 \text{m}^{-3} \text{yr}^{-1}$) estimated from the observational dataset and the uncertainty analyses using NorESM2-LM outputs (SAMPLE-UNC and TTD-UNC). For the analysis of the observational dataset and SAMPLE-UNC, values are the mean \pm one standard deviation of the $S_{\Delta\text{age}}^{\Delta\text{AOU}}$ distribution derived from the 625 analyses performed. The reference values in bracket are: for the SAMPLE-UNC analysis, $S_{\Delta\text{age}}^{\Delta\text{AOU}}$ computed with non-scarce data and, for the TTD-UNC analysis, $S_{\Delta\text{age}}^{\Delta\text{AOU}}$ derived using trends in ideal-age.

Analysis	Southern dense	Atlantic dense
Obs. dataset	0.04 ± 0.04	0.05 ± 0.01
SAMPLE-UNC	0.17 ± 0.04 (ref: 0.09)	0.18 ± 0.04 (ref: 0.14)
TTD-UNC	0.01 (ref: 0.10)	0.05 (ref: 0.13)

instances, trends may even oppose each other. In consequence, $S_{\Delta\text{age}}^{\Delta\text{AOU}}$ derived from observational data for the contemporary period are consistent with the lower range of estimates produced by ESMS. The reliability of these observational estimates for evaluating ESMS is compromised by the limited number of data points used in the estimation. However, increasing the number of data points by including non-significant trends yields only to minor changes in the estimations. In addition, given that $S_{\Delta\text{age}}^{\Delta\text{AOU}}$ is similar to some extent to an estimation of the oxygen utilisation rate (OUR) averaged within the TTD-mean-age is 0.01 and 0.05 $\text{mmolO}_2 \text{m}^{-3} \text{yr}^{-1}$ for the Southern dense and Atlantic dense water-masses considered, comparison with prior OUR estimates is appropriate. In the deep ocean, OUR estimations typically vary around 0.1, respectively (Table 2). This is 0.09 and 0.08 $\text{mmolO}_2 \text{m}^{-3} \text{yr}^{-1}$ (Sulpis et al., 2023). These observation-based estimations are also consistent with the lower range of the ESMS estimations lower than the reference values ($S_{\Delta\text{age}}^{\Delta\text{AOU}}$ derived from ideal-age). This suggests that the changes in simulated interior AOU may be overly sensitive to changes in age in most of the models analysed here. In addition, our analysis shows a relative stability over time of this sensitivity. This is likely an underestimation of the sensitivity on the future warmer period since observational studies has suggested increase remineralization and oxygen consumption with higher temperature (Brewer and Peltzer, 2017). These results indicates that the projected increase in AOU and thus $\text{DIC}_{\text{remin}}$ might be weaker for a similar increase in age. Hence, using trends in TTD-mean-age lead to underestimation of observation-based $S_{\Delta\text{age}}^{\Delta\text{AOU}}$ while the scarcity of data points and the need to compute trends in the T-S space results in overestimating it. Together, these overestimation and underestimation compromise the comparability of observation-based $S_{\Delta\text{age}}^{\Delta\text{AOU}}$ with $S_{\Delta\text{age}}^{\Delta\text{AOU}}$ derived from the ESMS.

4 Discussion

Our results highlight the importance of circulation changes on the changes in AOU and therefore on $\text{DIC}_{\text{remin}}$ in the deep ocean. Previous studies suggested that circulation was the main driver of changes in interior carbon content during the past and future climate (Bopp et al., 2017; Kessler et al., 2018; Liu and Primeau, 2023). We quantify that between 2015 and 2099, under the SSP5-8.5 climate change scenario, and in the ocean below 1000 metres, an increase in age contributes between and to an increase $\text{DIC}_{\text{remin}}$, based on MPI-ESM1.2-LR, MIROC-ES2L and NorESM2-LM whose $S_{\Delta\text{age}}^{\Delta\text{AOU}}$ are the closest to the observation-based estimates a circulation slow down contributes between 43 % and 106 % to the increase in $\text{DIC}_{\text{remin}}$. The densest water-mass coming from the Southern Ocean (southern dense water-mass) contribute predominantly to the deep ocean $\text{DIC}_{\text{remin}}$ increase. This water-mass covers a large portion of the deep ocean, and have particularly strong correlation between spatial fields of AOU trends and age trends and the contribution from the age increase is even larger ideal-age trends. While we highlight the importance of change in age ideal-age in this water-mass, a substantial portion of the change in AOU is not driven by change in age ideal-age in lighter water-masses, and question the reliability of using change in age as a proxy for change in AOU in the ocean above 2000 metres. Here, changes in export (Henson et al., 2022), spatially variable oxygen utilisation rate (Sulpis et al., 2023) or changes in remineralisation with temperature (Brewer and Peltzer, 2017) can de-correlate changes in AOU from changes in ideal-age. Here, changes in export (Henson et al., 2022), spatially variable Furthermore, in a transient climate, the conditions (strong advection over mixing and spatially even respiration) for a linear relationship between AOU trends and age trends can change over time. Changes in circulation can also recombine water masses differently bringing in waters with varying histories; waters can follow different pathways and go through different respiration fields

429 (Guo et al., 2023). In the lighter water masses and in the Atlantic dense water mass, changes in ideal-age explain a slightly
430 smaller portion of the spatial variability of AOU changes in the future compare to the contemporary period (weaker R^2),
431 suggesting caution when interpreting circulation changes from AOU.

432 On of the initial motivation for this work was to constrain ESM projections of AOU using changes in age. Our results suggest
433 that if we can constrain deep ocean ventilation changes then we can constrain projections of deep ocean AOU. However,
434 identifying the best ESMs at projecting deep ocean ventilation changes is challenging. For instance, under a different climate,
435 the last glacial maximum, ESMs simulate very different changes in Atlantic MOC (meridional overturning circulation) depth
436 and strength, and no ESM is consistent with the estimations from proxies (Sherriff-Tadano and Klockmann, 2021). On the
437 other hand, simulated changes in the North Atlantic circulation during stadial-interstadial climate transition show promising
438 comparison with proxy data (Waelbroeck et al., 2023). An accurate projection of the carbon sequestration by the BCP in the
439 deep ocean needs an accurate formation of the deep water-masses in the North Atlantic and Southern Ocean, yet it is not
440 possible to determine even one CMIP6 model that represents those accurately (Heuzé, 2021).

441 Constraining only circulation changes may not be enough to identify the best ESMs at projecting changes in AOU in the
442 interior ocean. The sensitivity of AOU changes to age changes varies substantially between ESMs (Fig. 3), modulating
443 circulation-driven changes in AOU. For instance, the slow down of the Southern and Atlantic MOC in MPI-ESM1.2-LR is
444 stronger compared to MIROC-ES2L (Liu et al., 2023), yet MPI-ESM1.2-LR shows the weakest change in ideal-age-driven
445 AOU trends and MIROC-ES2L the strongest one (Fig. 4). The linear relationship between present and future sensitivity across
446 ESMs is promising, in particular in the Southern dense water-mass which covers the largest portion of the deep ocean. It
447 can, in theory, be used to identify ESMs whose sensitivities are the most consistent with observations in the contemporary
448 period and be used to constrain the sensitivity of the future period. However, at this point in time, we cannot directly constrain
449 the sensitivity following an emergent constraint approach (Bourgeois et al., 2022; Kwiatkowski et al., 2017; Goris et al., 2023)
450 because of the small ESM ensemble available and the uncertainties in the observations based estimates.

451 The reliability of the $S_{\Delta\text{age}}^{\text{AAOU}}$ estimates from observational data is compromised by the limited number of data points and the
452 usage of the TTD method for estimating age trends. While the scarcity of data and the need to compute trends in T-S space lead
453 to a substantial overestimation when compared to a non-scarce data set, using trends in TTD-mean-age results in an equally
454 strong underestimation when compared to trends computed with ideal-age. While we are confident in our estimate of the first
455 uncertainty, we are more cautious regarding the evaluation of the second uncertainty (TTD method). In the model simulations,
456 in the ocean below 1000 metres, only the Southern Ocean and the North Atlantic are well-ventilated to the degree that the
457 CFC-12 concentrations can provide TTD-mean-age estimates. Thus, we can evaluate trends in TTD-mean-age against trends
458 in ideal-age only in these regions, representing a limited portion of the area covered by the observational dataset. Caution is
459 warranted when using TTD-mean-age to assess changes in ventilation, especially when TTD methods depend on assumptions
460 about the balance between advection and mixing (Δ/Γ). $\Delta/\Gamma = 1$ is a good compromise for the entire ocean but regionally
461 dependent Δ/Γ would lead to more optimal TTD-mean-age when compared to model (He et al., 2018). Approaches employing
462 dual constraint are promising and should be further explored (Guo et al., 2025). While imperfect, the estimates of $S_{\Delta\text{age}}^{\text{AAOU}}$ based
463 on scarce observational data and TTD-mean-age remain the only viable option for comparing $S_{\Delta\text{age}}^{\text{AAOU}}$ derived from ESMs. Given
464 that $S_{\Delta\text{age}}^{\text{AAOU}}$ is to some extent similar to an estimation of the oxygen utilisation rate (Sulpis et al., 2023) can de-correlate changes
465 in AOU from changes in age. averaged within the water-masses considered, comparison with prior observational-based OUR
466 estimates is appropriate. In the deep ocean, oxygen utilisation rate estimations typically vary around $0.1 \text{ mmol O}_2 \text{ m}^{-3} \text{ yr}^{-1}$
467 (Sulpis et al., 2023), substantially higher than the observation-based estimates from our work, yet on the lower end of the
468 $S_{\Delta\text{age}}^{\text{AAOU}}$ range derived from ESMs.

469 One caveat of our work is the use of AOU as a proxy of remineralised organic matter, notably as we focus on the deep ocean
470 where water parcels coming from the high latitude can be exported while being-undersaturated with respect to oxygen (Ito et al.,
471 2004; Duteil et al., 2013). Interestingly, when compared to true oxygen utilisation (TOU) that, which is a more accurate measure
472 of remineralised organic matter, AOU overestimates TOU but changes in AOU underestimates changes in TOU by 25 % (Koeve

473 et al., 2020). For our work, this suggests stronger trends in remineralised organic matter and thus stronger sensitivity of the
474 BCP to circulation slow-down relative to the sensitivity estimated from AOU trends in our ESM ensemble and the observation
475 baseline. This uncertainty is also linked to the physical representation biases in ESMs that strongly affect the projections
476 of interior oxygen changes (Ito et al., 2026), hence AOU. In addition, AOU underestimates organic matter remineralisation
477 because it does not account for denitrification occurring in suboxic waters. In global warming simulations, the volume of
478 suboxic waters increases all along the 20th and 21st century resulting in a small increase in denitrification (Fu et al., 2018;
479 Cocco et al., 2013). Nevertheless, since suboxic waters are mostly located in the upper 1000 metres of the ocean, the omission
480 of denitrification is expected to have a minimal impact on our results. If it does have an impact, it would likely result in a small
481 underestimation of $S_{\text{Age}}^{\text{AAOU}}$. Altogether, this highlights the need to consider the AOU uncertainty when inferred as a proxy for
482 remineralised organic matter in ESMs, calling for getting TOU outputs in future Coupled Model Intercomparison Project in
483 order to properly quantify the projected BCP changes.

484 5 Conclusion

485 One of the initial motivation for this work was to constrain ESMs projections of AOU based on the sensitivity of AOU changes
486 to age changes. The linear relationship between present and future sensitivity across ESMs is promising. It can, in theory, be
487 used to identify ESMs whose sensitivities are the most consistent with observations in the contemporary period and be used to
488 constrain the sensitivity. Understanding changes in ocean BCP and its impact on future climate change remains an outstanding
489 research question (Tjiputra et al., 2025). In this work, we have demonstrated that the spatial fields of AOU trends (an indicator
490 of changes in the BCP) and ideal-age trends are correlated in the ocean deeper than 1000 metres. Here, spatial variability in
491 ideal-age trends can explain more than half of the spatial variability in AOU trends ($R^2 > 0.5$). This relationship is identified in
492 simulations of the contemporary period (1982-2013) and simulations of the future period. However, at this point in time, we
493 cannot directly constrain AOU projections following an emergent constraint approach (Bourgeois et al., 2022; Kwiatkowski et al., 2017)
494 because of the small ESM ensemble available and the limitation of the currently available observations. Nonetheless, below
495 2000 metres, our results suggest that if we can constrain deep ocean ventilation changes then we can constrain projections of
496 deep ocean AOU. However, to identify the best ESMs at projecting deep ocean ventilation changes is challenging. For instance,
497 under a different climate, the last glacial maximum, ESMs simulate very different changes in Atlantic MOC (meridional
498 overturning circulation) depth and strength one from another and none of them is really consistent with the estimations from
499 proxies (Sherriff-Tadano and Kloekmann, 2021). On the other hand, simulated changes in the North Atlantic circulation during
500 stadial-interstadial climate transition show promising comparison with proxies data (Waelbroeck et al., 2023). In addition, constraining
501 only the changes in the MOC may not be enough to identify best ESMs at projecting changes in AOU in the interior ocean. The
502 uncertainties associated to interior ocean remineralization in the different models remain. For instance, the slow-down of the
503 Southern and Atlantic MOC in MPI-ESM1.2-LR is stronger compared to MIROC-ES2L (Liu et al., 2023), yet MPI-ESM1.2-LR
504 shows the weakest change in age-driven AOU trends and MIROC-ES2L the strongest one (Fig. ??). An accurate projection
505 of the carbon sequestration by the BCP in the deep ocean needs an accurate formation of the deep water masses in the North
506 Atlantic and Southern Ocean, yet it is not possible to determine even one CMIP6 model that represents those accurately
507 (Heuzé, 2021). (2015-2099) under the SSP5-8.5 climate change scenario. The sensitivity of AOU change to ideal-age change,
508 $S_{\text{Age}}^{\text{AAOU}}$ (that is, the slope of the linear regression), varies between the ESMs and the water-masses from 0.05 to 0.75 $\text{mmol O}_2 \text{ m}^{-3} \text{ yr}^{-1}$
509 for the contemporary period, depending on the ocean regions. $S_{\text{Age}}^{\text{AAOU}}$ remain relatively similar when computed for the 2015-2099
510 period. Using the linear relationship we estimate that, for the 2015-2099 time period, the increase in ideal-age, due to changes
511 in circulation or ventilation rates, contribute between 43 % and 106 % to the increase in deep ocean $\text{DIC}_{\text{remin}}$, which varies
512 between ESMs.

513 Disparities in deep ocean AOU changes across ESMs stem from differences in circulation changes and differences in the
514 sensitivity of AOU to these circulation changes. Constraining deep ocean AOU changes requires addressing both circulation
515 changes and sensitivities. Constraining sensitivities seems in reach, but would require a greater number of models providing

516 [ideal-age and preformed tracers, as well as expanding the observational database and refining the estimation of age changes](#)
517 [from ocean tracers](#). It is our hope that the ESMs represented in CMIP7 will offer further improvements compared to CMIP6 in
518 terms of their representation of ventilation, especially deep water formation. ~~We would like to emphasize that there is a need~~
519 ~~for more CMIP7 ESMs to run the simulations with an age and preformed tracers and to make the related outputs available,~~
520 [as well as available outputs](#) in the CMIP7 database. Given a larger model ensemble and more observations ~~with ongoing time,~~
521 our approach is a promising solution that would allow us to constrain the remineralised carbon sequestration in the deep ocean
522 for the next ~~CMIP7-generation~~ [ESM generations](#) to come. [Finally, while circulation-driven changes in deep ocean carbon](#)
523 [sequestration are substantial, they represent only one aspect of the overall process. Changes in biological processes also play](#)
524 [a substantial role, particularly in shallower ocean regions. Uncertainties associated to the biological processes driving interior](#)
525 [ocean remineralisation in the different models remain \(Henson et al., 2024\), deserving specific attention to understand carbon](#)
526 [sequestration in the intermediate depth ocean. Last but not least, constraining simulated changes in oxygen utilisation will also](#)
527 [be on step toward reconciling simulated and observed rates of current deoxygenation \(Ito et al., 2026\).](#)

528 [Authors contributions](#)

529 [Funding acquisition JT, Conceptualization and methodology DC, NG, SKL, JT, Formal analysis and visualization DC, XD,](#)
530 [Analysis of the results DC, XD, NG, EJ, SKL, JT, Writing \(original draft preparation\) DC, Writing \(review and editing\) DC,](#)
531 [XD, NG, EJ, SKL, JT.](#)

532 **Acknowledgements**

533 This work was funded by the European Union under grant agreement no. 101083922 (OceanICU). Views and opinions ex-
534 pressed are however those of the author(s) only and do not necessarily reflect those of the European Union or European
535 Research Executive Agency. Neither the European Union nor the granting authority can be held responsible for them. The
536 computational and storage resources were provided by Sigma2 - the National Infrastructure for High Performance Computing
537 and Data Storage in Norway (project no. NN1002K, NS1002K). The authors acknowledge the World Climate Research Pro-
538 gramme, which, through its Working Group on Coupled Modelling, coordinated and promoted CMIP6. The authors thank the
539 climate modelling groups for producing and making available their model output, the Earth System Grid Federation (ESGF)
540 for archiving the data and providing access, and the multiple funding agencies who support CMIP6 and ESGF. The authors ac-
541 knowledge the KeyCLIM project (grant 295046 from the Research Council of Norway) for coordinating access to the CMIP6
542 data. [The authors thank the two anonymous reviewers for their valuable feedbacks on the manuscript.](#)

543 **Data availability**

544 CMIP6 outputs are available from the Earth System Grid Federation (ESGF) portals (e.g. <https://esgf-node.ipsl.upmc.fr>). [The](#)
545 [observational dataset GLODAPv2 \(2016\) is available at https://doi.org/10.3334/cdiac/otg.ndp093_glodapv2 and the water mass](#)
546 [ages product at https://doi.org/10.25921/xp33-q351 \(Lauvset et al., 2023; Jeansson et al., 2021\).](#)

547 **Code availability**

548 The code for producing the figure is available at [https://github.com/damiencouespel/scripts-article-biological-carbon-pump-](https://github.com/damiencouespel/scripts-article-biological-carbon-pump-aou-trends-vs-age-trends)
549 [aou-trends-vs-age-trends](#).

Contributions

Funding acquisition JT, Conceptualization and methodology DC, NG, SKL, JT, Formal analysis and visualization DC, XD, Analysis of the results DC, XD, NG, EJ, SKL, JT, Writing (original draft preparation) DC, Writing (review and editing) DC, XD, NG, EJ, SKL, JT,

Competing interests

The authors declare no competing interests.

References

- L. A. Anderson and J. L. Sarmiento. Redfield ratios of remineralization determined by nutrient data analysis. *Global Biogeochemical Cycles*, 8(1):65–80, 1994. ISSN 1944-9224. doi: 10.1029/93GB03318.
- L. Bopp, L. Resplandy, A. Untersee, P. Le Mezo, and M. Kageyama. Ocean (de)oxygenation from the Last Glacial Maximum to the 21st century: Insights from Earth System Models. *Philosophical Transactions of the Royal Society A: Mathematical, Physical and Engineering Sciences*, 375(2102), 2017. doi: 10.1098/rsta.2016.0323.
- O. Boucher, J. Servonnat, A. L. Albright, O. Aumont, Y. Balkanski, V. Bastrikov, S. Bekki, R. Bonnet, S. Bony, L. Bopp, P. Braconnot, P. Brockmann, P. Cadule, A. Caubel, F. Cheruy, F. Codron, A. Cozic, D. Cugnet, F. D’Andrea, P. Davini, C. de Lavergne, S. Denvil, J. Deshayes, M. Devilliers, A. Ducharne, J.-L. Dufresne, E. Dupont, C. Éthé, L. Fairhead, L. Falletti, S. Flavoni, M.-A. Foujols, S. Gardoll, G. Gastineau, J. Ghattas, J.-Y. Grandpeix, B. Guenet, E. Guez, Lionel, E. Guilyardi, M. Guimberteau, D. Hauglustaine, F. Hourdin, A. Idelkadi, S. Joussaume, M. Kageyama, M. Khodri, G. Krinner, N. Lebas, G. Levavasseur, C. Lévy, L. Li, F. Lott, T. Lurton, S. Luysaert, G. Madec, J.-B. Madeleine, F. Maignan, M. Marchand, O. Marti, L. Mellul, Y. Meurdesoif, J. Mignot, I. Musat, C. Ottlé, P. Peylin, Y. Planton, J. Polcher, C. Rio, N. Rochetin, C. Rousset, P. Sepulchre, A. Sima, D. Swingedouw, R. Thiéblemont, A. K. Traore, M. Vancoppenolle, J. Vial, J. Vialard, N. Viovy, and N. Vuichard. Presentation and Evaluation of the IPSL-CM6A-LR Climate Model. *Journal of Advances in Modeling Earth Systems*, 12(7):e2019MS002010, 2020. ISSN 1942-2466. doi: 10.1029/2019MS002010.
- T. Bourgeois, N. Goris, J. Schwinger, and J. F. Tjiputra. Stratification constrains future heat and carbon uptake in the Southern Ocean between 30°S and 55°S. *Nature Communications*, 13(1):340, Jan. 2022. ISSN 2041-1723. doi: 10.1038/s41467-022-27979-5.
- P. W. Boyd, H. Claustre, M. Lévy, D. A. Siegel, and T. Weber. Multi-faceted particle pumps drive carbon sequestration in the ocean. *Nature*, 568(7752):327–335, Apr. 2019. ISSN 0028-0836. doi: 10.1038/s41586-019-1098-2.
- P. G. Brewer and E. T. Peltzer. Depth perception: The need to report ocean biogeochemical rates as functions of temperature, not depth. *Philosophical Transactions of the Royal Society A: Mathematical, Physical and Engineering Sciences*, 375(2102): 20160319, Aug. 2017. doi: 10.1098/rsta.2016.0319.
- W. S. Broecker, S. Blanton, W. M. Smethie Jr., and G. Ostlund. Radiocarbon decay and oxygen utilization in the Deep Atlantic Ocean. *Global Biogeochemical Cycles*, 5(1):87–117, 1991. ISSN 1944-9224. doi: 10.1029/90GB02279.
- W. S. Broecker, S. L. Peacock, S. Walker, R. Weiss, E. Fahrbach, M. Schroeder, U. Mikolajewicz, C. Heinze, R. Key, T.-H. Peng, and S. Rubin. How much deep water is formed in the Southern Ocean? *Journal of Geophysical Research: Oceans*, 103(C8):15833–15843, 1998. ISSN 2156-2202. doi: 10.1029/98JC00248.
- R. Caneill and A. Barna. Gsw-xarray. Zenodo, May 2024.

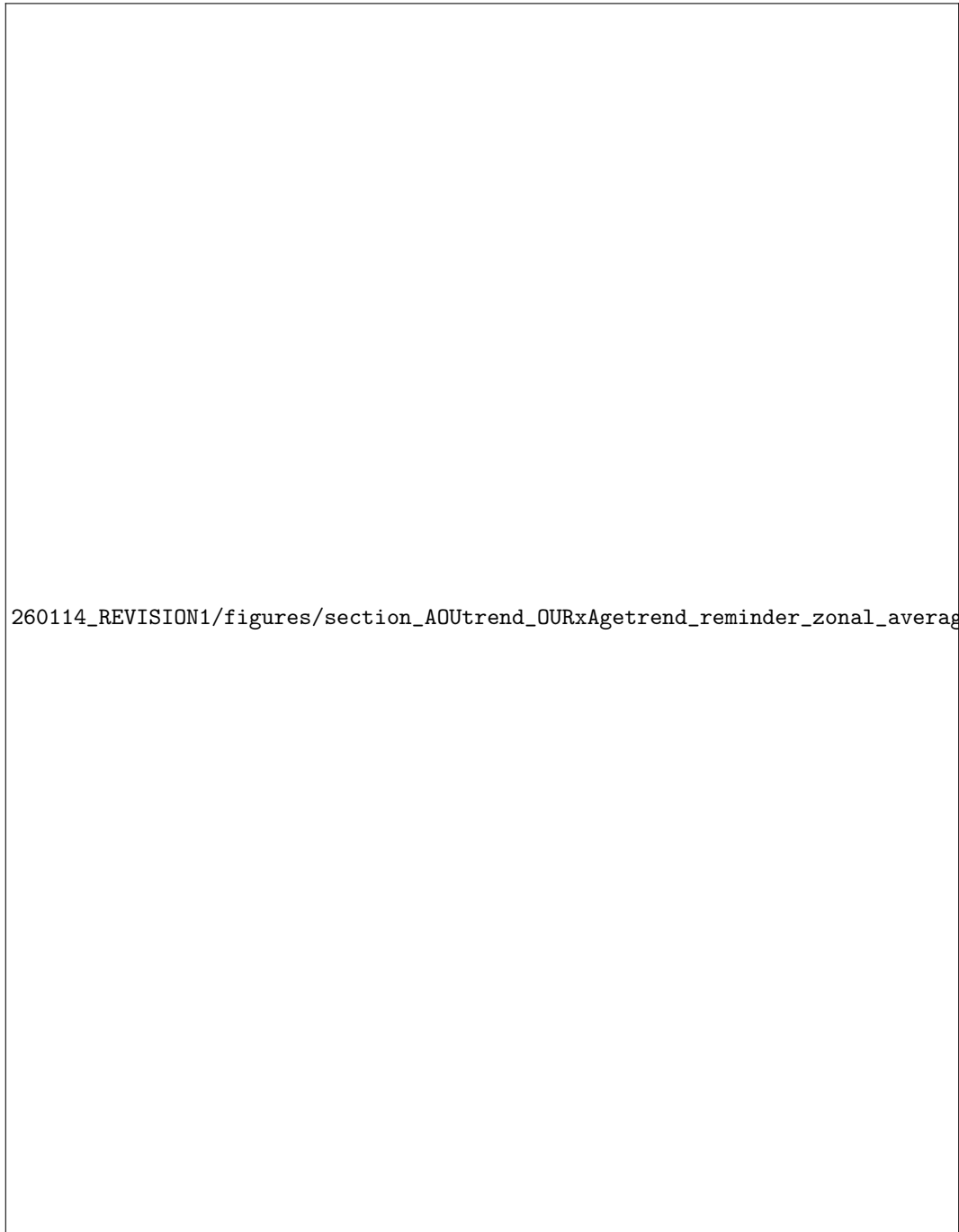
- 586 V. Cocco, F. Joos, M. Steinacher, T. L. Frölicher, L. Bopp, J. P. Dunne, M. Gehlen, C. Heinze, J. Orr, A. Oschlies, B. Schneider,
587 J. Segschneider, and J. Tjiputra. Oxygen and indicators of stress for marine life in multi-model global warming projections.
588 *Biogeosciences*, 10(3):1849–1868, 2013. doi: 10.5194/bg-10-1849-2013.
- 589 C. Deutsch, H. Brix, T. Ito, H. Frenzel, and L. Thompson. Climate-forced variability of ocean hypoxia. *Science*, 333(6040):
590 336–339, 2011. doi: 10.1126/science.1202422.
- 591 T. DeVries. The Ocean Carbon Cycle. *Annual Review of Environment and Resources*, 47(1):317–341, 2022. doi:
592 10.1146/annurev-environ-120920-111307.
- 593 J. P. Dunne, L. W. Horowitz, A. J. Adcroft, P. Ginoux, I. M. Held, J. G. John, J. P. Krasting, S. Malyshev, V. Naik, F. Paulot,
594 E. Shevliakova, C. A. Stock, N. Zadeh, V. Balaji, C. Blanton, K. A. Dunne, C. Dupuis, J. Durachta, R. Dussin, P. P. G.
595 Gauthier, S. M. Griffies, H. Guo, R. W. Hallberg, M. Harrison, J. He, W. Hurlin, C. McHugh, R. Menzel, P. C. D. Milly,
596 S. Nikonov, D. J. Paynter, J. Ploshay, A. Radhakrishnan, K. Rand, B. G. Reichl, T. Robinson, D. M. Schwarzkopf, L. T.
597 Sentman, S. Underwood, H. Vahlenkamp, M. Winton, A. T. Wittenberg, B. Wyman, Y. Zeng, and M. Zhao. The GFDL Earth
598 System Model Version 4.1 (GFDL-ESM 4.1): Overall Coupled Model Description and Simulation Characteristics. *Journal*
599 *of Advances in Modeling Earth Systems*, 12(11):e2019MS002015, 2020. ISSN 1942-2466. doi: 10.1029/2019MS002015.
- 600 O. Duteil, W. Koeve, A. Oschlies, D. Bianchi, E. Galbraith, I. Kriest, and R. Matear. A novel estimate of ocean oxygen
601 utilisation points to a reduced rate of respiration in the ocean interior. *Biogeosciences*, 10(11):7723–7738, Nov. 2013. ISSN
602 1726-4170. doi: 10.5194/bg-10-7723-2013.
- 603 R. A. Feely, C. L. Sabine, R. Schlitzer, J. L. Bullister, S. Mecking, and D. Greeley. Oxygen Utilization and Organic Carbon
604 Remineralization in the Upper Water Column of the Pacific Ocean. *Journal of Oceanography*, 60(1):45–52, Feb. 2004. ISSN
605 1573-868X. doi: 10.1023/B:JOCE.0000038317.01279.aa.
- 606 I. Frenger, A. Landolfi, K. Kvale, C. J. Somes, A. Oschlies, W. Yao, and W. Koeve. Misconceptions of the marine biological
607 carbon pump in a changing climate: Thinking outside the “export” box. *Global Change Biology*, 30(1):e17124, 2024. ISSN
608 1365-2486. doi: 10.1111/gcb.17124.
- 609 W. Fu, F. Primeau, J. Keith Moore, K. Lindsay, and J. T. Randerson. Reversal of increasing tropical ocean hypoxia trends with
610 sustained climate warming. *Global Biogeochemical Cycles*, 32(4):551–564, 2018. doi: 10.1002/2017GB005788.
- 611 H. Garcia and L. Gordon. Erratum: Oxygen solubility in seawater: Better fitting equations. *Limnology and Oceanography*, 38:
612 656, 1993.
- 613 H. E. Garcia and L. I. Gordon. Oxygen solubility in seawater: Better fitting equations. *Limnology and Oceanography*, 37(6):
614 1307–1312, 1992. doi: 10.4319/lo.1992.37.6.1307.
- 615 H. E. Garcia, Z. Wang, C. Bouchard, S. L. Cross, C. R. Paver, J. R. Reagan, T. P. Boyer, R. A. Locarnini, A. V. Mishonov,
616 O. K. Baranova, D. Seidov, and D. Dukhovskoy. World Ocean Atlas 2023, Volume 3: Dissolved Oxygen, Apparent Oxygen
617 Utilization, Dissolved Oxygen Saturation and 30-year Climate Normal. A. Mishonov Technical Editor. *NOAA Atlas NESDIS*
618 *91*, 2024. doi: 10.25923/rb67-ns53.
- 619 P. Goodwin, M. J. Follows, and R. G. Williams. Analytical relationships between atmospheric carbon dioxide, carbon emissions,
620 and ocean processes. *Global Biogeochemical Cycles*, 22(3), 2008. ISSN 1944-9224. doi: 10.1029/2008GB003184.
- 621 N. Goris, K. Johannsen, and J. Tjiputra. The emergence of the Gulf Stream and interior western boundary as key regions to
622 constrain the future North Atlantic carbon uptake. *Geoscientific Model Development*, 16(8):2095–2117, Apr. 2023. ISSN
623 1991-959X. doi: 10.5194/gmd-16-2095-2023.
- 624 H. Guo, I. Kriest, A. Oschlies, and W. Koeve. Can Oxygen Utilization Rate Be Used to Track the Long-Term Changes of
625 Aerobic Respiration in the Mesopelagic Atlantic Ocean? *Geophysical Research Letters*, 50(13):e2022GL102645, 2023.
626 ISSN 1944-8007. doi: 10.1029/2022GL102645.

- 627 H. Guo, W. Koeve, A. Oschlies, Y.-C. He, T. P. Kemena, L. Gerke, and I. Kriest. Dual-tracer constraints on the inverse Gaussian
628 transit time distribution improve the estimation of water mass ages and their temporal trends in the tropical thermocline.
629 *Ocean Science*, 21(3):1167–1182, July 2025. ISSN 1812-0784. doi: 10.5194/os-21-1167-2025.
- 630 T. Hajima, M. Watanabe, A. Yamamoto, H. Tatebe, M. A. Noguchi, M. Abe, R. Ohgaito, A. Ito, D. Yamazaki, H. Okajima,
631 A. Ito, K. Takata, K. Ogochi, S. Watanabe, and M. Kawamiya. Development of the MIROC-ES2L Earth system model and
632 the evaluation of biogeochemical processes and feedbacks. *Geoscientific Model Development*, 13(5):2197–2244, May 2020.
633 ISSN 1991-959X. doi: 10.5194/gmd-13-2197-2020.
- 634 Y.-C. He, J. Tjiputra, H. R. Langehaug, E. Jeansson, Y. Gao, J. Schwinger, and A. Olsen. A Model-Based Evaluation of the
635 Inverse Gaussian Transit-Time Distribution Method for Inferring Anthropogenic Carbon Storage in the Ocean. *Journal of*
636 *Geophysical Research: Oceans*, 123(3):1777–1800, Mar. 2018. ISSN 2169-9275, 2169-9291. doi: 10.1002/2017jc013504.
- 637 S. Henson, C. A. Baker, P. Halloran, A. McQuatters-Gollop, S. Painter, A. Planchat, and A. Tagliabue. Knowledge Gaps
638 in Quantifying the Climate Change Response of Biological Storage of Carbon in the Ocean. *Earth's Future*, 12(6):
639 e2023EF004375, 2024. ISSN 2328-4277. doi: 10.1029/2023EF004375.
- 640 S. A. Henson, C. Laufkötter, S. Leung, S. L. C. Giering, H. I. Palevsky, and E. L. Cavan. Uncertain response of ocean biological
641 carbon export in a changing world. *Nature Geoscience*, 15(4):248–254, Apr. 2022. ISSN 1752-0908. doi: 10.1038/s41561-
642 022-00927-0.
- 643 C. Heuzé. Antarctic Bottom Water and North Atlantic Deep Water in CMIP6 models. *Ocean Science*, 17(1):59–90, Jan. 2021.
644 ISSN 1812-0784. doi: 10.5194/os-17-59-2021.
- 645 T. Ito, M. J. Follows, and E. A. Boyle. Is AOU a good measure of respiration in the oceans? *Geophysical Research Letters*, 31
646 (17), 2004. ISSN 1944-8007. doi: 10.1029/2004GL020900.
- 647 T. Ito, Y. Takano, Y. A. Eddebbar, J. F. Tiputra, Z. Wang, S. Minobe, L. Cheng, J. Du, and Y. Abe. Are Simulated Ocean
648 Deoxygenation Rates Consistent with the Observational Reconstructions? *Annual Review Earth and Planetary Sciences*,
649 Jan. 2026. doi: 10.1146/annurev-earth-032524-123111.
- 650 E. Jeansson, R. Steinfeldt, and T. Toste. Water mass ages based on GLODAPv2 data product (NCEI Accession 0226793).
651 NOAA National Centers for Environmental Information., 2021.
- 652 E. Jeansson, T. Tanhua, A. Olsen, W. M. Smethie Jr., B. Rajasakaren, S. R. Ólafsdóttir, and J. Ólafsson. Decadal Changes in Ven-
653 tilation and Anthropogenic Carbon in the Nordic Seas. *Journal of Geophysical Research: Oceans*, 128(3):e2022JC019318,
654 2023. ISSN 2169-9291. doi: 10.1029/2022JC019318.
- 655 W. J. Jenkins. Oxygen utilization rates in North Atlantic subtropical gyre and primary production in oligotrophic systems.
656 *Nature*, 300(5889):246–248, Nov. 1982. ISSN 1476-4687. doi: 10.1038/300246a0.
- 657 R. F. Keeling, A. Körtzinger, and N. Gruber. Ocean deoxygenation in a warming world. *Annual review of marine science*, 2:
658 199–229, 2010. doi: 10.1146/annurev.marine.010908.163855.
- 659 A. Kessler, E. V. Galaasen, U. S. Ninnemann, and J. Tjiputra. Ocean carbon inventory under warmer climate conditions – the
660 case of the Last Interglacial. *Climate of the Past*, 14(12):1961–1976, Dec. 2018. ISSN 1814-9324. doi: 10.5194/cp-14-1961-
661 2018.
- 662 R. M. Key, A. Olsen, S. van Heuven, S. K. Lauvset, A. Velo, X. Lin, C. Schirnick, A. Kozyr, T. Tanhua, M. Hoppema,
663 S. Jutterström, R. Steinfeldt, E. Jeansson, M. Ishii, F. F. Perez, and T. Suzuki. Global Ocean Data Analysis Project, Version
664 2 (GLODAPv2), ORNL/CDIAC-162, NDP-093. Technical report, Carbon Dioxide Information Analysis Center, Oak Ridge
665 National Laboratory, US Department of Energy, Oak Ridge, Tennessee., 2015.

- 666 W. Koeve and P. Kähler. Oxygen utilization rate (OUR) underestimates ocean respiration: A model study. *Global Biogeochem-*
667 *ical Cycles*, 30(8):1166–1182, 2016. ISSN 1944-9224. doi: 10.1002/2015GB005354.
- 668 W. Koeve, P. Kähler, and A. Oschlies. Does Export Production Measure Transient Changes of the Biological Carbon Pump’s
669 Feedback to the Atmosphere Under Global Warming? *Geophysical Research Letters*, 47(22):e2020GL089928, 2020. ISSN
670 1944-8007. doi: 10.1029/2020GL089928.
- 671 L. Kwiatkowski, L. Bopp, O. Aumont, P. Ciais, P. M. Cox, C. Laufkötter, Y. Li, and R. Sférian. Emergent constraints on
672 projections of declining primary production in the tropical oceans. *Nature Climate Change*, 7(5):355–358, May 2017. ISSN
673 17586798. doi: 10.1038/nclimate3265.
- 674 L. Kwiatkowski, O. Torres, L. Bopp, O. Aumont, M. Chamberlain, J. R. Christian, J. P. Dunne, M. Gehlen, T. Ilyina, J. G.
675 John, A. Lenton, H. Li, N. S. Lovenduski, J. C. Orr, J. Palmieri, Y. Santana-Falcón, J. Schwinger, R. Sférian, C. A. Stock,
676 A. Tagliabue, Y. Takano, J. Tjiputra, K. Toyama, H. Tsujino, M. Watanabe, A. Yamamoto, A. Yool, and T. Ziehn. Twenty-first
677 century ocean warming, acidification, deoxygenation, and upper-ocean nutrient and primary production decline from CMIP6
678 model projections. *Biogeosciences*, 17(13):3439–3470, July 2020. ISSN 1726-4189. doi: 10.5194/bg-17-3439-2020.
- 679 E. Y. Kwon, F. Primeau, and J. L. Sarmiento. The impact of remineralization depth on the air–sea carbon balance. *Nature*
680 *Geoscience*, 2(9):630–635, Sept. 2009. ISSN 1752-0908. doi: 10.1038/ngeo612.
- 681 S. K. Lauvset, R. M. Key, A. Olsen, S. M. A. C. van Heuven, A. Velo, X. Lin, C. Schirnick, A. Kozyr, T. Tanhua, M. Hoppema,
682 S. Jutterström, R. Steinfeldt, E. Jeansson, M. Ishii, F. F. Pérez, T. Suzuki, and S. Watelet. A new global interior ocean mapped
683 climatology: The $1^\circ \times 1^\circ$ GLODAP version 2 from 1972-01-01 to 2013-12-31 (NCEI Accession 0286118). NOAA National
684 Centers for Environmental Information. Dataset., 2023.
- 685 S. K. Lauvset, N. Lange, T. Tanhua, H. C. Bittig, A. Olsen, A. Kozyr, M. Álvarez, K. Azetsu-Scott, P. J. Brown, B. R. Carter,
686 L. Cotrim da Cunha, M. Hoppema, M. P. Humphreys, M. Ishii, E. Jeansson, A. Murata, J. D. Müller, F. F. Pérez, C. Schirnick,
687 R. Steinfeldt, T. Suzuki, A. Ulfsbo, A. Velo, R. J. Woosley, and R. M. Key. The annual update GLODAPv2.2023: The global
688 interior ocean biogeochemical data product. *Earth System Science Data*, 16(4):2047–2072, Apr. 2024. ISSN 1866-3508.
689 doi: 10.5194/essd-16-2047-2024.
- 690 Y. Liu and F. Primeau. Surface-to-Interior Transport Timescales and Ventilation Patterns in a Time-Dependent Circulation
691 Driven by Sustained Climate Warming. *Journal of Physical Oceanography*, 54(1):173–186, Dec. 2023. ISSN 0022-3670,
692 1520-0485. doi: 10.1175/JPO-D-23-0113.1.
- 693 Y. Liu, J. K. Moore, F. Primeau, and W. L. Wang. Reduced CO₂ uptake and growing nutrient sequestration from slowing
694 overturning circulation. *Nature Climate Change*, 13(1):83–90, Jan. 2023. ISSN 1758-6798. doi: 10.1038/s41558-022-
695 01555-7.
- 696 E. Maier-Reimer, U. Mikolajewicz, and A. Winguth. Future ocean uptake of CO₂: Interaction between ocean circulation and
697 biology. *Climate Dynamics*, 12(10):711–721, 1996. ISSN 09307575. doi: 10.1007/s003820050138.
- 698 I. Marinov, A. Gnanadesikan, J. L. Sarmiento, J. R. Toggweiler, M. Follows, and B. K. Mignone. Impact of oceanic circulation
699 on biological carbon storage in the ocean and atmospheric pCO₂. *Global Biogeochemical Cycles*, 22(3):GB3007—n/a,
700 2008. doi: 10.1029/2007GB002958.
- 701 T. Mauritsen, J. Bader, T. Becker, J. Behrens, M. Bittner, R. Brokopf, V. Brovkin, M. Claussen, T. Crueger, M. Esch, I. Fast,
702 S. Fiedler, D. Fläschner, V. Gayler, M. Giorgetta, D. S. Goll, H. Haak, S. Hagemann, C. Hedemann, C. Hohenegger, T. Ily-
703 ina, T. Jahns, D. Jimenéz-de-la-Cuesta, J. Jungclaus, T. Kleinen, S. Kloster, D. Kracher, S. Kinne, D. Kleberg, G. Lass-
704 lop, L. Kornbluh, J. Marotzke, D. Matei, K. Meraner, U. Mikolajewicz, K. Modali, B. Möbis, W. A. Müller, J. E. M. S.
705 Nabel, C. C. W. Nam, D. Notz, S.-S. Nyawira, H. Paulsen, K. Peters, R. Pincus, H. Pohlmann, J. Pongratz, M. Popp,
706 T. J. Raddatz, S. Rast, R. Redler, C. H. Reick, T. Rohrschneider, V. Schemann, H. Schmidt, R. Schnur, U. Schulzweida,

- 707 K. D. Six, L. Stein, I. Stemmler, B. Stevens, J.-S. von Storch, F. Tian, A. Voigt, P. Vrese, K.-H. Wieners, S. Wilkenskjeld,
708 A. Winkler, and E. Roeckner. Developments in the MPI-M Earth System Model version 1.2 (MPI-ESM1.2) and Its Re-
709 sponse to Increasing CO₂. *Journal of Advances in Modeling Earth Systems*, 11(4):998–1038, 2019. ISSN 1942-2466. doi:
710 10.1029/2018MS001400.
- 711 T. J. McDougall and P. M. Barker. *Getting Started with TEOS-10 and the Gibbs Seawater (GSW) Oceanographic Toolbox*.
712 SCOR/IAPSO WG127, 2011. ISBN 978-0-646-55621-5.
- 713 M. S. Myksovoll, A. Britt Sandø, J. Tjiputra, A. Samuelsen, V. Çağlar Yumruktepe, C. Li, E. A. Mousing, J. P. H. Betten-
714 court, and G. Ottersen. Key physical processes and their model representation for projecting climate impacts on subarctic
715 Atlantic net primary production: A synthesis. *Progress in Oceanography*, 217:103084, Sept. 2023. ISSN 0079-6611. doi:
716 10.1016/j.pocean.2023.103084.
- 717 A. Olsen, R. M. Key, S. van Heuven, S. K. Lauvset, A. Velo, X. Lin, C. Schirnack, A. Kozyr, T. Tanhua, M. Hoppema,
718 S. Jutterström, R. Steinfeldt, E. Jeansson, M. Ishii, F. F. Pérez, and T. Suzuki. The Global Ocean Data Analysis Project
719 version 2 (GLODAPv2) – an internally consistent data product for the world ocean. *Earth System Science Data*, 8(2):
720 297–323, Aug. 2016. ISSN 1866-3508. doi: 10.5194/essd-8-297-2016.
- 721 J. L. Sarmiento and J. R. Toggweiler. A new model for the role of the oceans in determining atmospheric P CO₂. *Nature*, 308
722 (5960):621–624, Apr. 1984. ISSN 1476-4687. doi: 10.1038/308621a0.
- 723 J. L. Sarmiento, G. Thiele, R. M. Key, and W. S. Moore. Oxygen and nitrate new production and remineralization in the North
724 Atlantic subtropical gyre. *Journal of Geophysical Research: Oceans*, 95(C10):18303–18315, 1990. ISSN 2156-2202. doi:
725 10.1029/JC095iC10p18303.
- 726 R. Sférian, P. Nabat, M. Michou, D. Saint-Martin, A. Voldoire, J. Colin, B. Decharme, C. Delire, S. Berthet, M. Chevallier,
727 S. Sénési, L. Franchisteguy, J. Vial, M. Mallet, E. Joetzjer, O. Geoffroy, J.-F. Guérémy, M.-P. Moine, R. Msadek, A. Ribes,
728 M. Rocher, R. Roehrig, D. Salas-y-Mélia, E. Sanchez, L. Terray, S. Valcke, R. Waldman, O. Aumont, L. Bopp, J. Deshayes,
729 C. Éthé, and G. Madec. Evaluation of CNRM Earth System Model, CNRM-ESM2-1: Role of Earth System Processes in
730 Present-Day and Future Climate. *Journal of Advances in Modeling Earth Systems*, 11(12):4182–4227, 2019. ISSN 1942-
731 2466. doi: 10.1029/2019MS001791.
- 732 Ø. Seland, M. Bentsen, D. Olivie, T. Toniazzo, A. Gjermundsen, L. S. Graff, J. B. Debernard, A. K. Gupta, Y.-C. He,
733 A. Kirkevåg, J. Schwinger, J. Tjiputra, K. S. Aas, I. Bethke, Y. Fan, J. Griesfeller, A. Grini, C. Guo, M. Ilicak, I. H. H.
734 Karset, O. Landgren, J. Liakka, K. O. Moseid, A. Nummelin, C. Spensberger, H. Tang, Z. Zhang, C. Heinze, T. Iversen,
735 and M. Schulz. Overview of the Norwegian Earth System Model (NorESM2) and key climate response of CMIP6 DECK,
736 historical, and scenario simulations. *Geoscientific Model Development*, 13(12):6165–6200, Dec. 2020. ISSN 1991-959X.
737 doi: 10.5194/gmd-13-6165-2020.
- 738 A. A. Sellar, J. Walton, C. G. Jones, R. Wood, N. L. Abraham, M. Andrejczuk, M. B. Andrews, T. Andrews, A. T. Archibald,
739 L. de Mora, H. Dyson, M. Elkington, R. Ellis, P. Florek, P. Good, L. Gohar, S. Haddad, S. C. Hardiman, E. Hogan, A. Iwi,
740 C. D. Jones, B. Johnson, D. I. Kelley, J. Kettleborough, J. R. Knight, M. O. Köhler, T. Kuhlbrodt, S. Liddicoat, I. Linova-
741 Pavlova, M. S. Mizielski, O. Morgenstern, J. Mulcahy, E. Neiningner, F. M. O’Connor, R. Petrie, J. Ridley, J.-C. Rioual,
742 M. Roberts, E. Robertson, S. Rumbold, J. Seddon, H. Shepherd, S. Shim, A. Stephens, J. C. Teixeira, Y. Tang, J. Williams,
743 A. Wiltshire, and P. T. Griffiths. Implementation of U.K. Earth System Models for CMIP6. *Journal of Advances in Modeling*
744 *Earth Systems*, 12(4):e2019MS001946, 2020. ISSN 1942-2466. doi: 10.1029/2019MS001946.
- 745 S. Sherriff-Tadano and M. Klockmann. PMIP contributions to understanding the deep ocean circulation of the Last Glacial Max-
746 imum. *Past Global Changes Magazine*, 29(2):84–85, Nov. 2021. ISSN 2411605X, 24119180. doi: 10.22498/pages.29.2.84.
- 747 O. Sulpis, D. S. Trossman, M. Holzer, E. Jeansson, S. K. Lauvset, and J. J. Middelburg. Respiration Patterns in the Dark Ocean.
748 *Global Biogeochemical Cycles*, 37(8):e2023GB007747, 2023. ISSN 1944-9224. doi: 10.1029/2023GB007747.

- 749 N. C. Swart, J. N. S. Cole, V. V. Kharin, M. Lazare, J. F. Scinocca, N. P. Gillett, J. Anstey, V. Arora, J. R. Christian, S. Hanna,
750 Y. Jiao, W. G. Lee, F. Majaess, O. A. Saenko, C. Seiler, C. Seinen, A. Shao, M. Sigmond, L. Solheim, K. von Salzen, D. Yang,
751 and B. Winter. The Canadian Earth System Model version 5 (CanESM5.0.3). *Geoscientific Model Development*, 12(11):
752 4823–4873, Nov. 2019. ISSN 1991-959X. doi: 10.5194/gmd-12-4823-2019.
- 753 A. Tagliabue, L. Kwiatkowski, L. Bopp, M. Butenschön, W. Cheung, M. Lengaigne, and J. Vialard. Persistent Uncertainties in
754 Ocean Net Primary Production Climate Change Projections at Regional Scales Raise Challenges for Assessing Impacts on
755 Ecosystem Services. *Frontiers in Climate*, 3:738224, Nov. 2021. ISSN 2624-9553. doi: 10.3389/fclim.2021.738224.
- 756 J. L. Thomas, D. W. Waugh, and A. Gnanadesikan. Relationship between Age and Oxygen along Line W in the Northwest
757 Atlantic Ocean. *Ocean Science Journal*, 55(2):203–217, June 2020. ISSN 1738-5261, 2005-7172. doi: 10.1007/s12601-
758 020-0019-5.
- 759 J. F. Tjiputra, N. Goris, S. K. Lauvset, C. Heinze, A. Olsen, J. Schwinger, and R. Steinfeldt. Mechanisms and Early Detections
760 of Multidecadal Oxygen Changes in the Interior Subpolar North Atlantic. *Geophysical Research Letters*, 45(9):4218–4229,
761 2018. ISSN 1944-8007. doi: 10.1029/2018GL077096.
- 762 J. F. Tjiputra, J. Schwinger, M. Bentsen, A. L. Morée, S. Gao, I. Bethke, C. Heinze, N. Goris, A. Gupta, Y.-C. He, D. Olivie,
763 Ø. Seland, and M. Schulz. Ocean biogeochemistry in the Norwegian Earth System Model version 2 (NorESM2). *Geosci-
764 entific Model Development*, 13(5):2393–2431, May 2020. ISSN 1991-959X. doi: 10.5194/gmd-13-2393-2020.
- 765 J. F. Tjiputra, D. Couespel, and R. Sanders. Marine ecosystem role in setting up preindustrial and future climate. *Nature
766 Communications*, 16(1):1–8, Mar. 2025. ISSN 2041-1723. doi: 10.1038/s41467-025-57371-y.
- 767 P. Virtanen, R. Gommers, T. E. Oliphant, M. Haberland, T. Reddy, D. Cournapeau, E. Burovski, P. Peterson, W. Weckesser,
768 J. Bright, S. J. van der Walt, M. Brett, J. Wilson, K. J. Millman, N. Mayorov, A. R. J. Nelson, E. Jones, R. Kern, E. Larson,
769 C. J. Carey, Í. Polat, Y. Feng, E. W. Moore, J. VanderPlas, D. Laxalde, J. Perktold, R. Cimrman, I. Henriksen, E. A. Quintero,
770 C. R. Harris, A. M. Archibald, A. H. Ribeiro, F. Pedregosa, and P. van Mulbregt. SciPy 1.0: Fundamental algorithms for
771 scientific computing in Python. *Nature Methods*, 17(3):261–272, Mar. 2020. ISSN 1548-7105. doi: 10.1038/s41592-019-
772 0686-2.
- 773 T. Volk and M. I. Hoffert. Ocean carbon pumps: Analysis of relative strengths and efficiencies in ocean-driven atmospheric
774 CO₂ changes. *The Carbon Cycle and Atmospheric CO₂: Natural Variations Archean to Present. (1985)*, 32:99–110, 1985.
775 doi: 10.1029/GM032p0099.
- 776 C. Waelbroeck, J. Tjiputra, C. Guo, K. H. Nisancioglu, E. Jansen, N. Vázquez Riveiros, S. Toucanne, F. Eynaud, L. Rossignol,
777 F. Dewilde, E. Marchès, S. Lebreiro, and S. Nave. Atlantic circulation changes across a stadial–interstadial transition.
778 *Climate of the Past*, 19(5):901–913, May 2023. ISSN 1814-9324. doi: 10.5194/cp-19-901-2023.
- 779 W. Weijer, W. Cheng, O. A. Garuba, A. Hu, and B. T. Nadiga. CMIP6 Models Predict Significant 21st Century Decline
780 of the Atlantic Meridional Overturning Circulation. *Geophysical Research Letters*, 47(12):e2019GL086075, 2020. ISSN
781 1944-8007. doi: 10.1029/2019GL086075.
- 782 J. D. Wilson, O. Andrews, A. Katavouta, F. de Melo Viríssimo, R. M. Death, M. Adloff, C. A. Baker, B. Blackledge, F. W.
783 Goldsworth, A. T. Kennedy-Asser, Q. Liu, K. R. Sieradzan, E. Vosper, and R. Ying. The biological carbon pump in CMIP6
784 models: 21st century trends and uncertainties. *Proceedings of the National Academy of Sciences*, 119(29):e2204369119,
785 July 2022. doi: 10.1073/pnas.2204369119.
- 786 T. Ziehn, M. A. Chamberlain, R. M. Law, A. Lenton, R. W. Bodman, M. Dix, L. Stevens, Y.-P. Wang, and J. Srbinovsky.
787 The Australian Earth System Model: ACCESS-ESM1.5. *Journal of Southern Hemisphere Earth Systems Science*, 70(1):
788 193–214, Aug. 2020. ISSN 2206-5865. doi: 10.1071/ES19035.



260114_REVISION1/figures/section_AOUtrend_OURxAgetrend_reminder_zonal_average.png

Figure 5. Zonally averaged trend in apparent oxygen utilisation ($\frac{d\Delta\text{AOU}}{dt}$, first column) and the contribution from trends in ideal-age ($S_{\text{Age}}^{\Delta\text{AOU}} \times \frac{d\text{age}}{dt}$, second column) under the SSP5-8.5 climate change scenario simulated with five Earth system models: MPI-ESM1.2-LR, ACCESS-ESM1.5, IPSL-CM6A-LR, MIROC-ES2L, NorESM2-LM. The remainder ($B + \epsilon$, third column) is computed as the difference between the two aforementioned components (see Eq. 3). Trends are computed for the period from 2015 to 2099 and are zonally averaged on the four water-masses considered in this study, accounting only for grid points with significant trends (p-value > 0.05).